

## Key Points:

- Magnetic pore fabrics can complement X-ray tomography, to capture small pores, and assess field-scale variations in pore fabrics
- A total shape ellipsoid is derived from X-ray tomography data, to represent average pore orientation and shape, and minimize artifacts
- The principal directions of magnetic pore fabrics and total shape ellipsoids are generally coaxial in most samples

## Supporting Information:

Supporting Information may be found in the online version of this article.

## Correspondence to:

Y. Zhou,  
yi.zhou@geo.unibe.ch

## Citation:

Zhou, Y., Pugnetti, M., Foubert, A., Lanari, P., Neururer, C., & Biedermann, A. R. (2022). Quantitative comparison of 3D pore space properties with magnetic pore fabrics—testing the ability of magnetic methods to predict pore fabrics in rocks. *Geochemistry, Geophysics, Geosystems*, 23, e2022GC010403. <https://doi.org/10.1029/2022GC010403>

Received 22 FEB 2022

Accepted 1 SEP 2022

© 2022. The Authors.

This is an open access article under the terms of the [Creative Commons Attribution License](#), which permits use, distribution and reproduction in any medium, provided the original work is properly cited.

## Quantitative Comparison of 3D Pore Space Properties With Magnetic Pore Fabrics—Testing the Ability of Magnetic Methods to Predict Pore Fabrics in Rocks

Y. Zhou<sup>1</sup> , M. Pugnetti<sup>1</sup>, A. Foubert<sup>2</sup>, P. Lanari<sup>1</sup> , C. Neururer<sup>2</sup>, and A. R. Biedermann<sup>1</sup> 

<sup>1</sup>Institute of Geological Sciences, University of Bern, Bern, Switzerland, <sup>2</sup>Department of Geosciences, University of Fribourg, Fribourg, Switzerland

**Abstract** Pore fabrics characterize the anisotropy of pore space in rocks and influence the direction of fluid flow. This is important in reservoir characterization, and petroleum and geothermal energy exploitation. X-ray computed micro-tomography (XRCT) is commonly used to analyze pore fabrics, but limited by the micron-scale resolution for representative 1-inch rock cores. The magnetic pore fabric (MPF) method has been proposed to capture pores down to 10 nm. Although empirical relationships between MPF and pore space properties or permeability anisotropy are available, their application is compromised by large variability. This study integrates He pycnometry and XRCT-derived pore space models with MPFs, and provides a quantitative comparison for calcarenite (~50 vol% porosity and complex pore structure), and molasse sandstone (10%–30% porosity and relatively homogeneous pore fabrics). The preferred orientation of pores obtained from XRCT is described by a total shape ellipsoid, calculated by summing the second-order tensors reflecting the best-fit ellipsoids of individual pores. This ellipsoid is then compared to the MPF magnitude ellipsoid in terms of fabric orientation, degree and shape of anisotropy. The MPF and total shape ellipsoids are generally coaxial. The MPF has a smaller anisotropy degree than the total shape ellipsoid, and their relationship depends on the ferrofluid properties. The anisotropy shapes show large variability. Nevertheless, the good agreement of principal directions in most samples makes MPFs a valuable and efficient complementary tool to analyze a large number of samples, in combination with XRCT on selected samples, for a field-scale pore space characterization.

**Plain Language Summary** Understanding underground fluid flow is a major goal when exploring geothermal energy and the migration of petroleum. These fluids transfer between pores at multiple scales. When the pores are flattened or elongated and display a preferred orientation, fluids will flow more readily in some directions compared to others. This results in preferred flow directions and flow paths. In this study, a fast way of determining pore geometry based on magnetic measurements is compared to traditional characterization methods. The good agreement between results suggests that magnetic methods can be applied as a complementary tool to include larger numbers of samples and potentially capture pores not resolved by traditional methods, with important implications for studies in geology and geological engineering.

### 1. Introduction

The fabric of connected pores, that is, their shape, orientation, and connectivity, largely controls rock properties such as permeability. An accurate 3D description of pore fabrics has therefore many applications, including geothermal energy usage (Aliyu & Chen, 2018; Frosch et al., 2000; Wagner et al., 2005; Zhang, Liu, et al., 2020), hydrocarbon exploitation, especially in tight rock (Chen et al., 2020; Gao & Hu, 2018; Kibria et al., 2018; Lai et al., 2018; Sun et al., 2021; Yang et al., 2017, 2018; Zhang, Liu, et al., 2020), and numerical simulations of fluid flow in reservoirs (Mehmani et al., 2020; Wang et al., 2009; Yang et al., 2019; Zhang et al., 2015). Pore fabrics can be characterized directly or indirectly, as defined below.

Direct methods provide maps or grids of the pore network: (a) Image analysis of optical microscopy thin sections has a resolution of ~0.23 μm at best for 2D observations (Andriani & Walsh, 2002; Gustafsson, 2000; Heintzmann & Ficiz, 2013; Ingham, 2010). Sample preparation may destroy or alter pores or create pseudo-pores if grains are detached during polishing (Heilbronner & Barrett, 2013). (b) Scanning electron microscopy (SEM) is a 2D mapping technique that can image pores down to 1–10 nm (Bultreys et al., 2016; Reed, 2005), characterizing a limited number of micropores within a single plane (De Boever et al., 2015; Marszałek et al., 2014; Mavris et al., 2012; Vázquez et al., 2013). (c) X-ray computed micro-tomography (XRCT) has emerged as a 3D technique

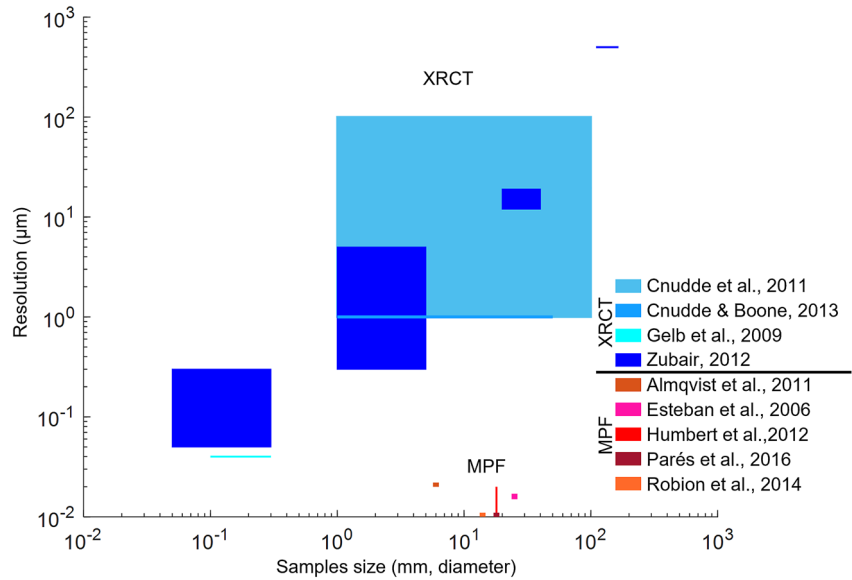


**Figure 1.** Sample size (diameter of the cylindrical core) versus resolution for X-ray computed micro-tomography (XRCT) and magnetic pore fabric (MPF) methods (XRCT modified from Cnudde & Boone, 2013; Cnudde et al., 2011; Gelb et al., 2009; Zubair, 2012). The MPF resolution is 10–20 nm for sample sizes ranging from 6 to 25.4 mm diameter (Almqvist et al., 2011; Esteban et al., 2006; Humbert et al., 2012; Parés et al., 2016; Robion et al., 2014).

to characterize the internal structure of rocks including their pore fabric, and provides the basis for digital rock physics (DRP) models that predict physical properties of rocks, especially acoustic and flow properties (Andrá et al., 2013; Holzer et al., 2011; Madadi & Varslot, 2009; Madonna et al., 2012; Pini, 2016). Zhan et al. (2009) and Zubair (2012) reported a good fit between numerical calculation and direct porosity and permeability measurements using Berea sandstone and carbonate rocks. A crucial prerequisite for meaningful comparisons between model and measurement is that both are conducted on representative sample volumes. Sample sizes ranging from sub-micrometers to a few centimeters are commonly used for XRCT (Cnudde & Boone, 2013; da Silva, 2018; Gelb et al., 2009; Landis & Keane, 2010; Zubair, 2012). Larger samples may be more representative of the investigated rock, but suffer from lower spatial resolution (Figure 1). Unresolved pores can result in up to 32% difference between modeled and measured data (Zhan et al., 2009).

Indirect methods characterize pore fabrics by measuring the anisotropy of specific physical properties influenced by pore fabrics, for example, permeability and seismic anisotropy and magnetic anisotropy of samples impregnated by ferrofluid. They provide average information on pore space properties, which is sufficient for many applications (e.g., Almqvist et al., 2011). Note that although permeability anisotropy is considered an indirect measurement of pore fabric, it is the most direct assessment of a rock's fluid transport properties. Permeability anisotropy is a symmetric second-order tensor, requiring at least six independent directional measurements for full description (Coulson & Nye, 1958). Otherwise, a priori information on the fabric orientation is needed, for example, lineation and foliation directions, in case that measured directions disagree with the principal permeability directions, thus underestimating permeability anisotropy. Another indirect description for pore fabric is elastic anisotropy. However, elasticity is a fourth-order tensor, thus requiring a large number of directional measurements or symmetry assumptions. Analogously to permeability anisotropy, each directional velocity is generally measured along a separate oriented core. Moreover, seismic velocities are affected by microcracks, grain boundaries and intrinsic elastic anisotropy of each grain in addition to pore fabrics, so seismic-based pore space characterization is challenging (Benson et al., 2003; David et al., 2017; Louis et al., 2004; Robion et al., 2014).

Magnetic pore fabrics (MPFs) provide a fast and efficient tool for pore fabric characterization. The samples' pore space is impregnated with ferrofluid, followed by measuring the anisotropy of magnetic susceptibility (AMS) (Pfleiderer & Halls, 1990), and thus only connected pores, which contribute to flow, are targeted by MPFs. MPFs can be applied on a single sample, without any priori information on the fabric, thus avoiding underestimating anisotropy by heterogeneity. Additionally, the method has been ascribed the ability to capture pores and pore

throats down to 10–20 nm (Figure 1) (Almqvist et al., 2011; Esteban et al., 2006; Humbert et al., 2012; Parés et al., 2016; Robion et al., 2014). Pores and throats smaller than magnetic nanoparticles (10–20 nm diameter) are not captured by MPF. In practice, the threshold of pores that are impregnated depends on pore throat geometry and wettability (Robion et al., 2014), and 100 nm has been put forward as a more realistic threshold (Pugnetti et al., 2022). Empirical relationships have been established between MPFs and pore fabrics: (a) the maximum and minimum principal susceptibility axes are sub-parallel to the average orientations of major and minor pore axes (Hrouda et al., 2000; Jezek & Hrouda, 2007; Jones et al., 2006; Pfliegerer & Halls, 1990, 1994), (b) the degree of magnetic anisotropy increases when pore shapes become more anisotropic (Jones et al., 2006; Pfliegerer & Halls, 1990, 1993; Robion et al., 2014), and (c) oblate or prolate MPFs are related to flattened or elongated pore shapes (Jones et al., 2006; Pfliegerer & Halls, 1990). MPFs have been compared to permeability anisotropy (Benson et al., 2003; Hailwood et al., 1999; Louis et al., 2005; Nabawy et al., 2009; Pfliegerer & Halls, 1994), and used to predict anisotropy of elastic properties (Almqvist et al., 2011). Unfortunately, empirical relationships vary largely between different studies, making the results hard to interpret (Almqvist et al., 2011; Benson et al., 2003; Jones et al., 2006; Louis et al., 2005; Nabawy et al., 2009; Pfliegerer & Halls, 1990, 1993, 1994; Robion et al., 2014). The variability may be explained partly by that large pores contain large volumes of ferrofluid, whereas the preferred orientation of pore connections is more relevant for permeability anisotropy (Pfliegerer & Halls, 1994). Pore shape, orientation and arrangement control MPFs, and ferrofluid susceptibility and measurement conditions largely influence MPF–pore fabric relationships (Biedermann, 2019; Biedermann et al., 2021). Many MPF studies focused on simplified samples (Biedermann, 2019; Jones et al., 2006; Pfliegerer & Halls, 1990), and factors affecting the relationships between MPFs and pore space in natural samples are not yet fully understood.

Two complementary pore fabric characterization methods are investigated and correlated quantitatively in terms of the portion of pore space they characterize, and obtained fabric orientation, degree and shape: XRCT as a standard method, and MPF which has great potential but is rarely used. Two sedimentary rocks, calcarenite and molasse, were included with variability in porosity and pore complexity. A new second-order tensor quantity, the total shape ellipsoid, is derived from XRCT data, for direct comparison with MPF in terms of fabric orientation, anisotropy degree and shape.

## 2. Materials and Methods

### 2.1. Sample Description

Samples with porosity of 10%–55% were chosen, molasse and calcarenite, applying for typical porosity of reservoir rocks varying between 5% and 40% (Guo, 2019; Monicard, 1980). Ideally, a single rock type would have been used for all porosities to minimize the number of variables. Because the collected molasse samples have 10%–30% porosity with micropores, calcarenite with large pores was included, extending the porosity range to ~50%.

The studied calcarenites are Plio-Pleistocene in age and recovered from the Gravina Formation in Apulia, Italy (Figure 2a) (Oryem et al., 2015). They possess high porosity (16%–60%) and a large proportion of interconnected pores (>99.5% of pore space on average) (Ciantia et al., 2015). Different pore types are identified in BSE images, such as inter- and intragranular porosity, microporosity, and moldic porosity (Figure 2b). Calcarenite cores MI-1-Z3, MI-2-Y3, MI-2-Y8, MI-2-Y10, MI-3-X15, MI-3-X11 were drilled from the same block along three perpendicular directions, indicated by X, Y and Z in the sample names. Samples MI-5-Z21 and MI-5-X22 were drilled from another block. Molasse sandstone was collected in four areas from the Upper Marine Molasse (OMM) in the Swiss molasse basin (SMB): (a) Rüggenberg, BE, samples D1121Z, D1112Y, D1263Y2, D1234X, D1221X, D1261X, (b) Entlebuch, LU, samples C43Y, C334Y, BE42AY, (c) Dürdingen, FR, Switzerland, sample 5256X, and (d) Tafers, FR, Switzerland, sample F31Z1 (Figure 2c). The molasse samples are characterized by cross and parallel bedding (Figure 2d). OMM consists mainly of shallow marine and tidal-influenced sandstones and mudstones, deposited in a shallow seaway from 20 to 17 Ma (Chevalier et al., 2010; Garefalakis & Schlunegger, 2019). The OMM sandstone displays porosities from 5% to 20% (Chevalier et al., 2010; Schegg et al., 1997), mainly including intergranular porosity and microporosity (Figure 2d). Being an important aquifer in the SMB, OMM may provide pore space to store and transfer CO<sub>2</sub> and geothermal fluids (Chelle-Michou et al., 2017; Chevalier et al., 2010; Kohl et al., 2010; Rybach, 2019). All rocks were drilled and cut to obtain standard-sized cores of 25.4 mm diameter and 22 mm length. Initial sample characterization involved porosity

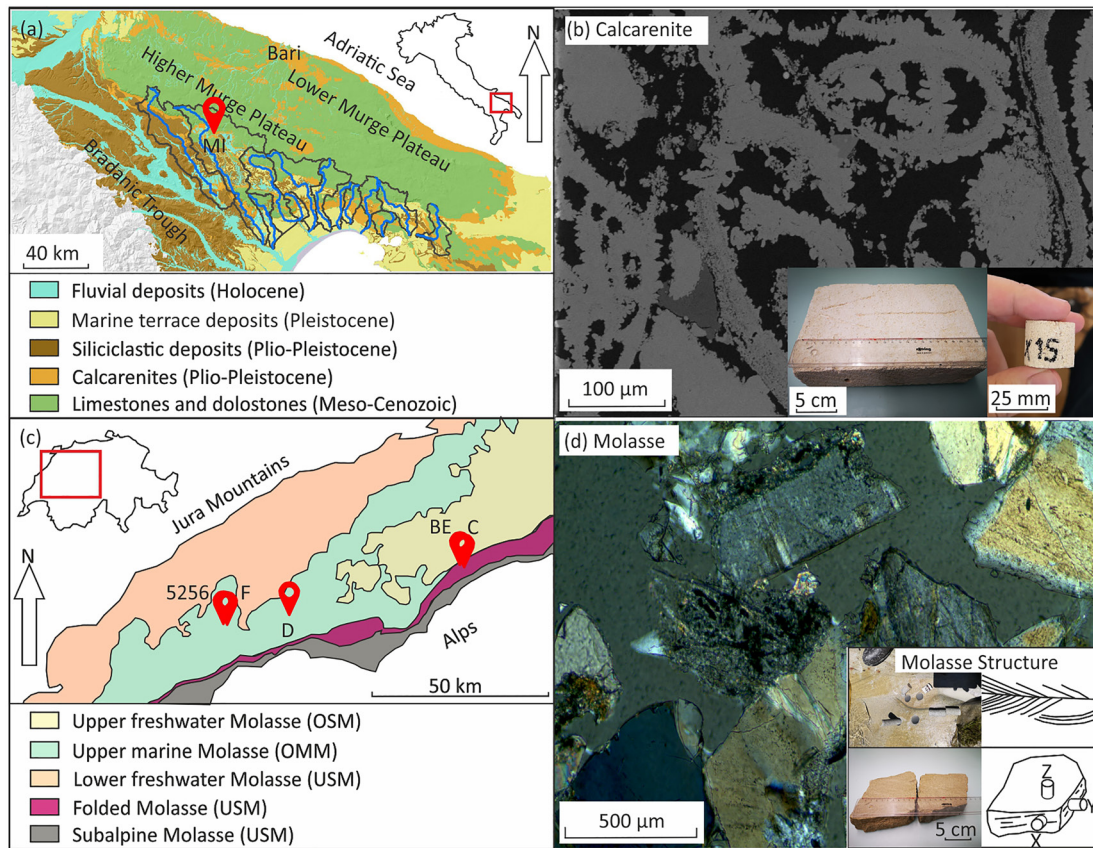


**Figure 2.** (a) Location of calcarenite samples, (b) Backscattered electron image of calcarenite sample and photograph of calcarenite sample and core, (c) location of molasse samples, (d) thin section image and photograph of molasse sandstone with sketch on internal structure and drilling directions. Note the cross-stratification in the molasse sandstone. The core axis was generally oriented parallel or perpendicular to lineation, provided that lineation could be clearly identified. Coordinates of MI are  $40^{\circ}49'14.5''\text{N}$ ,  $16^{\circ}25'25.0''\text{E}$ ; for D  $46^{\circ}49'45.6''\text{N}$ ,  $7^{\circ}24'04.4''\text{E}$ ; for C  $46^{\circ}58'52.4''\text{N}$ ,  $8^{\circ}03'48.3''\text{E}$ ; for BE  $46^{\circ}58'54.3''\text{N}$ ,  $8^{\circ}03'47.7''\text{E}$ ; for 5256  $46^{\circ}48'11.2''\text{N}$ ,  $7^{\circ}10'51.2''\text{E}$ , and for F  $46^{\circ}48'09.8''\text{N}$ ,  $7^{\circ}11'00.9''\text{E}$ . All molasse samples are OMM, even though mainly USM is present in the area where samples C and BE were obtained. Geological maps are modified after Donnalioia et al. (2019) (a), Sommaruga et al. (2012) and Wirth et al. (2020) (c).

measurements by comparing grain volume (obtained from a Micromeritics AccuPyc 1340 Automatic Gas (He) Pycnometer system in the Petrophysics Laboratory at the University of Bern) with bulk volume (calculated by core diameter and length).

## 2.2. XRCT Data Acquisition and Processing

The Bruker SkyScan 2211 3D X-ray micro-tomography scanner perform initial scans at the University of Fribourg (15  $\mu\text{m}$  pixel size), and a Bruker SkyScan 1273 obtain later measurements at the University of Bern (9  $\mu\text{m}$  or 5.5  $\mu\text{m}$  pixel size). Samples D1112Y and C334Y were measured on both systems for different resolution (Table S1 in Supporting Information S1). However, the direct comparison between both systems was not performed for all samples, as part of them (MI-1-Z3, MI-2-Y3, MI-2-Y10, MI-3-X15, MI-3-X11, D1121Z, D1234X, D1221X, D1261X, C43Y, and BE42AY) were impregnated or destructively analyzed after initial scanning with the Bruker Skyscan 2211, while others (MI-2-Y8, MI-5-Z21, MI-5-X22, D1263Y2, and 5256X, F31Z1) were measured only on the SkyScan 1273 for later analysis. XRCT data of impregnated samples were not further analyzed due to impregnation rendering the segmentation between ferrofluid/resin and solid fraction difficult. Rather, additional cores, so-called sister samples, were drilled from the original block in close proximity, assuming that both cores represent the same pore fabric. Pairs of sister samples are given as Core1/Core2, where XRCT data were obtained on the first core, and MPF on the second, for example, MI-3-X15/MI-3-X11. Where possible, XRCT data were obtained on Core1, and MPF data were obtained on both sister samples, allowing to test between-sample heterogeneity, for example, MI-2-Y8/MI-2-Y10 and D1234X/D1221X. Sample MI-2-Y3 was

drilled along the same direction as MI-2-Y8/MI-2-Y10 but further away, and similar situation for D1261X with D1234X/D1221X. The D12 block has a visible macroscopic fabric, parallel bedding, and thus similar pore fabrics are expected for samples along the same orientation.

Initially, different filters, voltage, current, and exposure time were used on each sample, in accordance with minor changes in their physical properties. Conditions for the X-ray source on the Bruker Skyscan 2211 were 80 kV/230  $\mu$ A for the calcarenites, and 100–156 kV/200–445  $\mu$ A for the molasse sandstones. Filters of 0.5 mm Al, 0.5 mm Ti, 0.5 mm Mo and 0.5 mm Cu were chosen for different samples. Images were acquired at 220 ms exposure time for calcarenite, and 100–300 ms for the molasse sandstone (Table S1 in Supporting Information S1). Different settings resulted in different contrast and artifacts, which could be corrected and removed during the reconstruction. Then it became evident that one consistent set of settings was sufficient for all samples to obtain images with good contrast and reduced artifacts. Only resolution was decisive in defining image quality. Settings on the Bruker Skyscan 1273 were the same for all samples with 100 kV/80  $\mu$ A, 1 mm Al + 0.038 mm Cu filter, and 275 ms exposure time (Table S1 in Supporting Information S1). Reconstructions were performed using NRecon, and images were compensated for misalignment, corrected for ring artifacts and beam hardening artifacts (Skyscan, 2011).

After reconstruction, the unsharp masking filter (Polesel et al., 2000; Strobel, 1996) was applied to noisy images, to sharpen and enhance image details in Avizo versions 2019.4 and 2020.1. Single thresholding segmentation was applied to differentiate pores from the solid fraction based on the attenuation coefficients, expressed as grayscale values (Figure 3). Because the determination of a threshold value is user-dependent and affects the segmentation of pixels with intermediate values (Andrä et al., 2013; Karimpouli & Tahmasebi, 2019; Sun et al., 2017; Thomson et al., 2018), a watershed segmentation was applied to assign intermediate grayscale values (Bieniek & Moga, 2000). The uncertainties in calculated porosity were estimated by testing different thresholds (Figure S1 in Supporting Information S1).

To ensure the representativeness of the volume for XRCT-derived calculations while minimizing computational cost, the representative elementary volume (REV) was determined, by calculating porosity (defined as relative abundance of pixels with grayscale values identified as pores) or pore size distributions as a function of included volume. Porosity and pore size distribution were calculated for cubes of increasing size, from  $100 \times 100 \times 100$  voxels ( $0.9 \times 0.9 \times 0.9$  mm<sup>3</sup>) to  $500 \times 500 \times 500$  voxels. For small volumes, XRCT-derived parameters vary largely with increasing volume, reaching a plateau as cube size increases above a critical threshold. This threshold volume is the REV, that is, the smallest volume representing the entire sample. Note that the REV can vary depending on the property of interest. Here, the REV for determining porosity is  $100 \times 100 \times 100$  voxels (cf. Figure 3), while for pore size distributions, the REV is  $300 \times 300 \times 300$  voxels (Figures 4a and 4b). To further estimate the uncertainty associated with sample heterogeneity, calculated porosities from five  $5 \times 5 \times 5$  mm<sup>3</sup> cubes located at different positions within the sample were compared to calculate a mean porosity with deviation (Table 1). Then, one cube was chosen arbitrarily for pore shape analysis (Figure 3).

The segmented pore space was separated into individual pores to characterize pore shape and size distribution (Gostick, 2017; Soille, 2000). Pore size is given as equivalent diameter of a sphere with the same volume. Individual pores are approximated with best-fit ellipsoids, represented mathematically by symmetric second-order tensors whose eigenvalues  $a \geq b \geq c$  correspond to the lengths of the major, intermediate and minor ellipsoid axes, and the eigenvectors  $V_1$ ,  $V_2$ , and  $V_3$  describe their orientations (Figure 3 and Text S1 in Supporting Information S1) (Avizo, 2020). Pore fabrics are traditionally characterized by orientation density functions (ODFs) of the major and minor pore axes (Dullien, 1979). In the present study, ODFs are however strongly affected by artifacts arising from small pores whose geometry remained unresolved. A series of filters was applied to remove pores smaller than  $4 \times 4 \times 4$  voxels up to  $16 \times 16 \times 16$  voxels, to investigate related changes in the ODFs. Additional difficulties inherent to the characterization of major and minor axes by ODFs are that all pores contribute equally, independent of size, and the lack of information on pore shape. For example, in a strongly elongated pore, the minor and intermediate axes may be similar, so that the orientation of the minor axis is poorly defined.

An alternative approach to analyze the average pore fabric is introduced here to reduce these difficulties: the total shape ellipsoid, which is calculated by adding the unnormalized second-order tensors reflecting individual pores. Advantages of the total shape ellipsoid include: (a) The calculation was adapted from averaging normalized second-order tensors to compute a mean anisotropy of a group of samples (Jelínek & Kropáček, 1978).

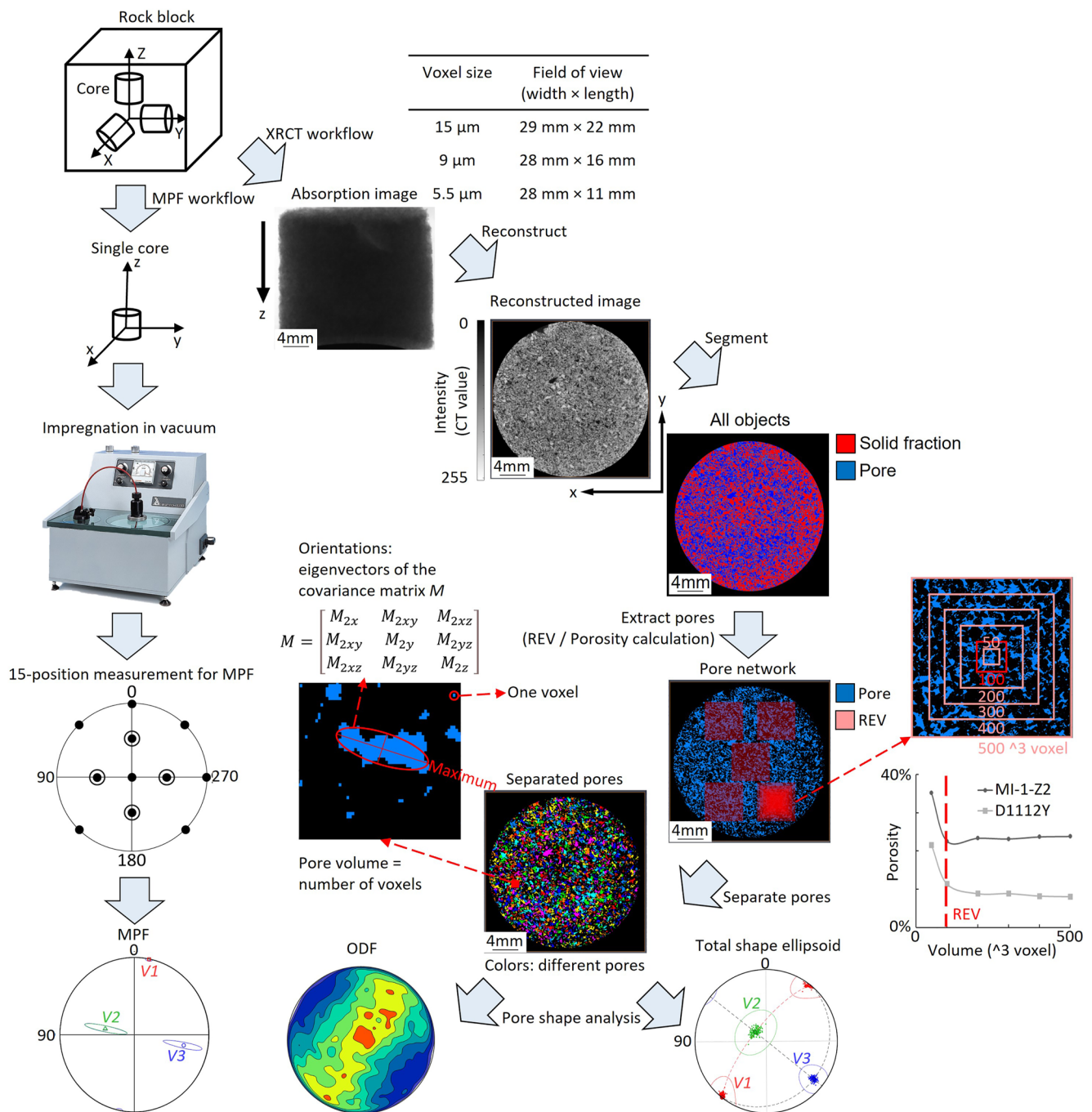


**Figure 3.** Workflow for X-ray computed micro-tomography image processing and magnetic pore fabric (MPF). The samples are scanned in field of view to obtain 28–29 mm width of images. Increasing voxel sizes are related to increasing fields of view. For 5.5 μm voxel size, results of two scans are stitched together after scanning in two horizontal positions. Absorption images are converted to cross-section images of greyscale CT intensity values during reconstruction. Hierarchical watershed segmentation divides the reconstructed volume into pores (blue) and solid fraction (red). Once the pore network is extracted from the segmented image, the bulk pore space is separated using the Skeleton-Aggressive algorithm which creates a connectivity network between the individual pores based on nodes and throats. The representative elementary volume is selected based the relationship between calculated porosity and sample size. The individual pore size is given as the equivalent diameter (EqDiameter) of a sphere that has the same volume as the pore, and the shape and orientation are defined by eigenvectors and eigenvalues of the covariance matrix  $M$  (a second-order tensor) (Text S1 in Supporting Information S1) (Avizo, 2020). The orientation density functions and total shape ellipsoids are derived from the matrices of single pores. The cores are impregnated by ferrofluid before measuring MPF.

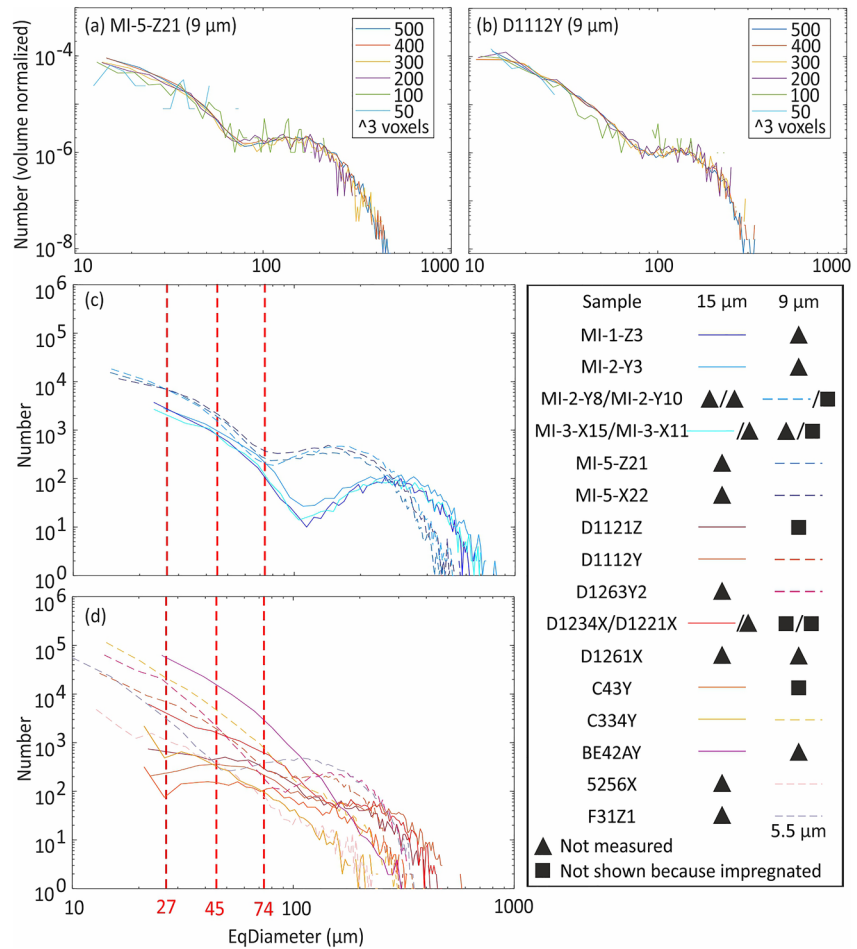


**Figure 4.** Results of pore size distribution for all X-ray computed micro-tomography scans. (a) and (b) present changes in pore size distribution associated with changing the included volume for calcarenite MI-5-Z21 and molasse D1112Y. The representative elementary volume for pore size distribution is  $300^3$  voxels for both because the  $300^3$  voxels are the minimum volume to present similar pore size distribution. If the volume is smaller than  $300^3$  voxels, there are not enough pores to present the full range of distribution, and hence maxima and minima vary. (c) and (d) are pore size distributions for different calcarenites and molasse sandstones. The pore size is given as the equivalent diameter (EqDiameter) of a sphere that has the same volume as the pore. Only data obtained prior to impregnation are shown. The red vertical lines represent the threshold of  $4 \times 4 \times 4$  voxels (EqDiameter = 27  $\mu\text{m}$  for voxel size of  $5.5^3 \mu\text{m}^3$ , or 45  $\mu\text{m}$  for voxel size of  $9^3 \mu\text{m}^3$ , or 74  $\mu\text{m}$  for  $15^3 \mu\text{m}^3$  voxel size).

Normalized tensors ensure that each contribution has the same weight, so that the average is controlled by the most anisotropic item. Unnormalized tensors allow to give more weight to larger and better defined pores, and minimize resolution-related artifacts compared to ODFs; (b) the orientation distribution, pore shape distribution, and distribution of aspect ratios are integrated in one single measure; and (c) the total shape ellipsoid can be directly compared to other second-order tensor properties, including permeability and MPF. Finally, because the total shape ellipsoid is calculated from a large number of individual pores, its statistical robustness can be assessed by bootstrapping (Constable & Tauxe, 1990; Tauxe et al., 1998). Here, 500 total shape ellipsoids were calculated from randomly and repetitively choosing subsets including 579–14,913 pores for different samples and resolutions (Hext, 1963; Jelínek & Kropáček, 1978; Owens, 2000). Finally, confidence ellipses were calculated based on those bootstrapped total shape ellipsoids and plotted by TomoFab (Petri et al., 2020).

The anisotropy of the individual pores as well as that of the total shape ellipsoid are described by the anisotropy degree  $P_s = a/c$ , and their shape by  $U_s = (2*b - a - c)/(a - c)$ . The definitions are analogous to standard parameters used for the characterization of magnetic anisotropy,  $P_m = k1/k3$  and  $U_m = (2*k2 - k1 - k3)/(k1 - k3)$ , where  $k1 \geq k2 \geq k3$  are the principal susceptibilities (Jelinek, 1981).  $P_m$  and  $P_s$  range in the interval (1,  $\infty$ ),

**Table 1**  
*Porosity Comparison of Numerical Calculations Based on XRCT Data, Laboratory Measurements by He Pycnometry and Estimation From MPF*

Sample	Porosity (resolution: 15 $\mu\text{m}$ /Skyscan 2211) (%) (threshold for pores, 0–255)	Porosity (resolution: 9 $\mu\text{m}$ /Skyscan 1273) (%) (threshold for pores, 0–255)	Porosity (He pycnometry, AccuPyc 1340) (%)	Porosity (MPF) (%)
<b>Calcarenite</b>				
MI-1-Z3	43 $\pm$ 4 (70)	▲	52 $\pm$ 1	29.4
MI-2-Y3	36 $\pm$ 4 (73)	▲	51.6 $\pm$ 0.3	46.0
MI-2-Y8/MI-2-Y10	▲/▲	33 $\pm$ 3 (74)/■	53.1 $\pm$ 0.4/55.2 $\pm$ 0.5	15.5/28.7
MI-3-X15/MI-3-X11	31 $\pm$ 5 (65)/▲	▲/■	51.2 $\pm$ 0.4/54.7 $\pm$ 0.3	▲/28.9
MI-5-Z21	▲	35 $\pm$ 3 (71)	55.2 $\pm$ 0.2	17.5
MI-5-X22	▲	34 $\pm$ 5 (68)	53.8 $\pm$ 0.2	12.7
<b>Molasse (Rüeggisberg)</b>				
D1121Z	5 $\pm$ 2 (45)	■	19.04 $\pm$ 0.02	25.6
D1112Y	6 $\pm$ 3 (45)	6 $\pm$ 1 (45)	20.78 $\pm$ 0.03	11.8
D1263Y2	▲	9 $\pm$ 2 (55)	21.78 $\pm$ 0.01	3.84
D1234X/D1221X	9 $\pm$ 3 (55)/▲	■/■	19.01 $\pm$ 0.01/20.29 $\pm$ 0.01	10.7/9.26
D1261X	▲	▲	20.26 $\pm$ 0.02	5.55
<b>Molasse (Entlebuch)</b>				
C43Y	4 $\pm$ 4 (60)	■	16.0 $\pm$ 0.2	7.63
C334Y	0.6 $\pm$ 0.1 (55)	1.9 $\pm$ 0.8 (60)	13.5 $\pm$ 0.7	5.60
BE42AY	6.4 $\pm$ 0.5 (65)	▲	12.05 $\pm$ 0.01	6.69
<b>Molasse (Düdingen)</b>				
5256X	▲	4 $\pm$ 1 (60)	11.13 $\pm$ 0.01	▲
<b>Molasse (Tafers)</b>				
F31Z1	▲	16.4 $\pm$ 1 (5.5 $\mu\text{m}$ ) (68)	30.78 $\pm$ 0.07	9.22

*Note.* Uncertainty was estimated by calculating the standard deviation of five cube volumes ( $5 \times 5 \times 5 \text{ mm}^3$ ) in five positions (XRCT—X-ray computed micro-tomography) or the standard deviation of five measurements (He pycnometry). Triangle indicates data not measured and square indicates data not shown because they were measured after impregnation.

where 1 means isotropy and increasing values relate to increasing degrees of anisotropy. The values of  $U_m$  and  $U_s$  vary in the range  $(-1, 1)$ , where  $-1$  describes rotationally prolate ellipsoids and  $+1$  indicates rotationally oblate ellipsoids.

To investigate how different pore size windows affect pore fabrics, the fabrics of pores with EqDiameter  $\geq 100$  and  $\leq 100 \mu\text{m}$  in sample MI-3-X15 were compared.

### 2.3. Magnetic Pore Fabric Measurements

The AMS of the dry samples was measured using a 15 directions measurement scheme to determine the anisotropy of the rock itself (Jelinek, 1977). Two instruments were used, the magnetic susceptibility bridge SM150 from ZH instruments (Czech Republic) for initial measurements, followed by the MFK1-FA susceptibility bridge from AGICO (Czech Republic). The measurement frequencies were set to  $\sim 4$ ,  $\sim 16$ , and  $\sim 512 \text{ kHz}$  for the SM150, using a field of 80 A/m, the maximum available at all frequencies. On the MFK1-FA, frequencies of  $\sim 1$ ,  $\sim 4$ ,  $\sim 16 \text{ kHz}$  were used with the standard field of 200 A/m. Five repeated measurements were obtained for every direction at each frequency, to increase data quality and assess the significance of anisotropy against the instrumental noise level (Biedermann et al., 2013). The noise level of the MFK1-FA is orders of magnitude lower than that of the SM150, so that the former is able to detect anisotropy where the latter cannot. Therefore, samples were

remeasured on the MFK1-FA, except MI-1-Z3 and MI-2-Y3, which had been cut after impregnation to check the spatial variability of impregnation efficiency.

After characterizing their initial anisotropy, samples MI-1-Z3, MI-2-Y3 and MI-3-X15 were impregnated with oil-based ferrofluid (EMG 909 with an intrinsic susceptibility of 1.38 SI) diluted at 1:25 volume ratio of ferrofluid to light hydrocarbon carrier oil offered by Ferrotec. These samples were impregnated under vacuum for 24 hr at 100 kPa, following the technique outlined in Parés et al. (2016). After initial experiments had shown difficulties with impregnation efficiency, the remaining samples were impregnated with oil-based ferrofluid diluted by resin and hardener (hardener:resin = 1:4) under vacuum for 1 hr at 100 kPa. As the resin solidifies, it is thought to keep the magnetic nanoparticles immobile within the pores (Thorpe et al., 2016). Ferrofluid was diluted at volume ratio of 1:50 for molasse MI-2-Y10, MI-3-X11, D1121Z, D1112Y, D1234X, D1221X, C43Y, BE42AY, F31Z1 and 1:30 for the remaining molasse, and all calcarenite samples (Table S2 in Supporting Information S1). Any resin-ferrofluid mixture on the surface of the sample was cleaned before solidification to avoid artifacts. Unfortunately, the elimination was not thorough for samples MI-2-Y8, MI-5-X22, MI-5-Z21, D1263Y2, D1261X and C334Y, resulting in artifacts during MPF measurements. These samples were polished to remove leftover resin from the surface. Samples MI-3-X15 and 5256X broke during the impregnation experiment. New experiments will be performed once more sophisticated impregnation methods are available (Pugnetti et al., 2021).

To test which proportion of the pore space was impregnated, the susceptibility of impregnated samples was compared to the independently measured susceptibility of diluted ferrofluid and ferrofluid-resin mixtures. From this, the ferrofluid porosity, and susceptibility-based impregnation efficiencies were calculated (Parés et al., 2016). The susceptibility was divided by a coefficient 1–1.3 for 512–1 kHz to correct frequency dependence (Biedermann et al., 2021). The MPFs were measured as magnetic anisotropy after impregnation, following the same protocol as for AMS described above. Samples MI-1-Z3 and MI-2-Y3 were measured at 4, 16 and 512 kHz on the SM150. Samples MI-3-X11, D1121Z, D1234X and C43Y were measured at 1 kHz, 4 and 16 kHz on the MFK1-FA, and all remaining samples were measured at 1 kHz on the MFK1-FA, once it became clear that anisotropy is higher and better defined at lower frequency (Biedermann et al., 2021).

The data quality and statistical significance of the anisotropy compared to instrument noise for AMS and MPF are described by  $R1$  (Biedermann et al., 2013) as well as confidence angles  $E13$  ( $=E31$ ),  $E12$  ( $=E21$ ) and  $E23$  ( $=E32$ ) based on the 15 mean directional susceptibilities (Hext, 1963; Jelinek, 1977, 1981). Large  $R1$  values and small confidence angles indicate significant anisotropy and well-defined directions. Note that magnetic anisotropy measurements on dry samples are called AMS in this study, whereas the term MPF is used to indicate results on the impregnated samples. The susceptibility of the dry calcarenite samples is  $\sim 3$  orders of magnitude lower than that of the impregnated samples, and a factor of 4–10 lower for dry compared to impregnated molasse samples. Additionally, the AMS is not significant in many of the investigated rocks. Therefore, the AMS can be neglected, and only the MPF results will be discussed further.

#### 2.4. Correlation of XRCT and MPF Data

The size range of pores captured by XRCT or MPFs is different, and they yield different types of data: XRCT provides a grid of voxels identified as pores, whereas the MPF is an average representation of the overall pore fabric. Nevertheless, they can be compared when calculating a total shape ellipsoid, which represents the pore fabric of all pores larger than  $4 \times 4 \times 4$  voxels. Both total shape ellipsoids and MPFs are second-order tensors and represent the entire sample volume, which allows a direct comparison of fabric orientation, as well as the anisotropy degree and shape parameters. Abbreviations used as subscript are explained in Table S3 in Supporting Information S1. Note that the MPF  $P$ -value depends on the intrinsic susceptibility of the fluid used for impregnation in addition to the average pore shape (Biedermann, 2019; Jones et al., 2006). Therefore,  $P_m$  will always be lower than  $P_s$ , and it is also expected to be lower when the ferrofluid was more diluted. Nevertheless, an increase in  $P_m$  with increasing  $P_s$  is expected as long as the susceptibility of the fluid is constant.

### 3. Results

#### 3.1. XRCT Results

##### 3.1.1. 3D Reconstructions and Porosity

The calcarenites present 31%–43% XRCT-derived porosities and 51.2%–55.2% He porosities, and molasse sandstones have 0.6%–16.4% XRCT-derived porosities and 11.13%–30.78% He porosities (Table 1). There is no clear and uniquely defined limit in gray-scale values that distinguishes pores and solid fraction, due to averaging of the attenuation coefficients of pore and matrix in voxels containing a mix of both. Adjustment of the threshold value from 73 to 85 causes a change in calculated porosity for the calcarenite MI-2-Y3 of ~10% (Figure S1 in Supporting Information S1). Additionally, pore throats are narrower than pores and thus harder to resolve by XRCT, leading to overestimating the isolated porosity and underestimating the connected porosity. The discrepancy between XRCT and He porosities is larger for molasse samples than calcarenites, due to the smaller pore size of molasse, resulting in a larger fraction of pores being below the spatial resolution of XRCT. These small pores are included in the He porosity, indicating that 46%–95% of the pore space in molasse sandstones and 17%–43% for calcarenites are not resolved by the XRCT data.

##### 3.1.2. Pore Size Distributions

The REV of pore size distribution was presented above (Figures 4a and 4b). Note that additional pores smaller than the voxel resolution ( $5.5^3 \mu\text{m}^3$ ,  $9^3 \mu\text{m}^3$  or  $15^3 \mu\text{m}^3$ ) may be presented. The different resolutions cause different datasets. Between 1% and 22% of the identified pores occupy a small number of voxels, generating unresolved shape and orientation. A lower threshold of  $4 \times 4 \times 4$  voxels was chosen for orientation and shape analyses, including 78%–99% of the XRCT-derived pore space and <83% of the pore space defined by He pycnometry. Calcarenites display bimodal pore size distributions, with two maxima at ~20 and ~300  $\mu\text{m}$  equivalent pore diameter for samples measured with 15- $\mu\text{m}$  pixel size or at ~12 and ~150  $\mu\text{m}$  for samples with 9- $\mu\text{m}$  pixel size, as the range of pore sizes detected depends on the resolution. Molasse sandstones have a unimodal pore size distribution, where 95%–99% of micropores (1%–22% of the pore volume) have sizes below the threshold for shape/orientation resolution. For samples D1112Y and C334Y measured at both resolutions, additional micropores are identified at higher resolution, and C334Y also displays additional large pores at higher resolution (Figure 4).

##### 3.1.3. Pore Orientation

As the orientation of pores below a certain size limit cannot be resolved, causing extreme maxima parallel to the sample  $x$ ,  $y$  and  $z$ -axes when including all identified pores for analysis. These artifacts are reduced when increasing the lower threshold of analyzed pore sizes from  $4 \times 4 \times 4$  voxels to  $16 \times 16 \times 16$  voxels at the expense of diminishing the number of included pores. The total shape ellipsoids appear unaffected by these artifacts, and display similar orientations and anisotropy degrees, even when including the large number of small pores (66%–84% of the number of XRCT-derived pores but 1%–5% of XRCT-derived pore volume) (Figure 5a).

##### 3.1.3.1. Calcarenite

All samples whose names start with MI-1, MI-2 and MI-3 were drilled from the same block, in perpendicular directions. For MI-1-Z3,  $V1_{s\text{-individual}}$  group sub-parallel to the sample  $x$ -axis. The minor axes  $V3_{s\text{-individual}}$  form a girdle distribution in the  $yz$ -plane, with a sub-maximum parallel to  $z$ . The bootstrapped total shape ellipsoid displays a similar  $V1_{s\text{-total}}$  direction (at  $36^\circ$  from the sample  $x$ -axis), and the mean  $V3_{s\text{-total}}$  direction is at  $26^\circ$  to the sample  $y$ -axis (Figure 5a). A comparison of the total shape ellipsoid with individual pore orientations shows that  $V3_{s\text{-total}}$  is defined by the absence of  $V1_{s\text{-individual}}$  axes rather than a grouping of  $V3_{s\text{-individual}}$ . Sister samples MI-2-Y8/MI-2-Y10, and MI-2-Y3 were drilled in the same orientation, but display different fabric orientations. In MI-2-Y3,  $V1_{s\text{-individual}}$  show a girdle distribution in the  $yz$ -plane with three sub-maxima, and  $V3_{s\text{-individual}}$  group closely around  $z$ . The orientation of total shape ellipsoid, with  $V3_{s\text{-total}}$  at  $33^\circ$  to the  $x$ -axis and broad distributions of  $V1_{s\text{-total}}$  and  $V2_{s\text{-total}}$ , is dominantly controlled by the  $V1_{s\text{-individual}}$  distribution (Figure 5b). Conversely, the  $V1_{s\text{-individual}}$  axes of sample MI-2-Y8 show a girdle distribution within a plane rotated  $\sim 30^\circ$  from the  $xz$ -plane around the  $z$ -axis, and  $V3_{s\text{-individual}}$  axes are grouped at  $\sim 30^\circ$  to the  $y$ -axis in the  $xy$ -plane. The  $V1_{s\text{-total}}$  and  $V2_{s\text{-total}}$  axes show a broad distribution in the plane defined by the  $V1_{s\text{-individual}}$  girdle (Figure 5c). For MI-3-X15, both  $V1_{s\text{-individual}}$  and  $V1_{s\text{-total}}$  are sub-parallel to the  $z$ -axis. The  $V3_{s\text{-individual}}$  and  $V3_{s\text{-total}}$  directions group close to the  $y$ -axis. For EqDiameter  $\leq 100$  and  $\geq 100 \mu\text{m}$  of pores,  $V3_{s\text{-total}}$  axes of both size windows are close to the  $y$ -axis and  $V1_{s\text{-total}}$  and  $V2_{s\text{-total}}$  are in the  $xz$ -plane (Figure 5d).

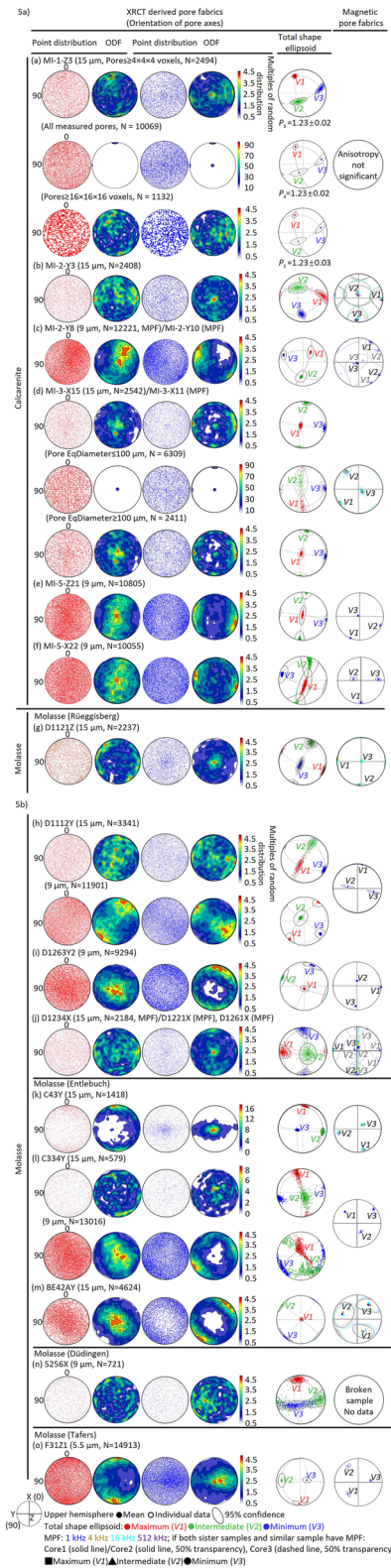


Figure 5.

Samples MI-5-Z21 and MI-5-X22 were drilled from a second block, and their orientations are mutually perpendicular, but unrelated to previous calcarenite samples. Nevertheless, they show similar pore fabrics:  $V3_{s\text{-individual}}$  and  $V3_{s\text{-total}}$  group sub-parallel to  $y$ , and  $V1_{s\text{-individual}}$  groups sub-parallel to  $z$ , defining  $V1_{s\text{-total}}$  (Figures 5e and 5f).

The calcarenites MI-1-Z3, MI-2-Y3, MI-2-Y8 and MI-3-X15 are mutually perpendicular, and can be used to assess how representative fabrics on cores are for the entire block. If the block is perfectly homogeneous, the total shape ellipsoids should coincide once all datasets in a common coordinate system. After rotating all datasets to the sample coordinates of MI-1-Z3, the  $V1_{s\text{-total}}$  axes of MI-1-Z3, MI-2-Y3, MI-2-Y8, and MI-3-X15 are at  $9^\circ\text{--}36^\circ$  to the  $x$ -axis, but are statistically distinct at 95% confidence. The orientations of  $V2_{s\text{-total}}$  and  $V3_{s\text{-total}}$  axes are largely variable (Figure S2 in Supporting Information S1). Additionally, the type of grouping is different for each sample: in MI-1-Z3, the  $V1_{s\text{-total}}$  form a point distribution, whereas the  $V3_{s\text{-total}}$  form a point distribution in MI-3-X15. This indicates between-sample heterogeneity, and implies that a large number of standard-sized samples would need to be measured and averaged to obtain a pore fabric representative of this rock.

### 3.1.3.2. Molasse

Samples D11 and D12 were drilled from two different blocks collected at the same site. Samples C43Y and C334Y were also drilled from blocks from the same location, but with different orientations. Sample 5256X was from another block. For molasse D1121Z, the  $V3_{s\text{-individual}}$  and  $V3_{s\text{-total}}$  group around the  $z$  direction, and the  $V1_{s\text{-individual}}$  present a girdle distribution in the  $xy$  plane, which is also reflected by the total shape ellipsoid (Figure 5g). Sample D1121Y was measured at both resolutions, 15- and 9- $\mu\text{m}$ , and both datasets show girdle distributions of  $V1_{s\text{-individual}}$  and  $V1_{s\text{-total}}$  axes rotated  $\sim 30^\circ$  around the  $z$ -axis from the  $xz$ -plane. The directions for  $V3_{s\text{-individual}}$  and  $V3_{s\text{-total}}$  group at  $\sim 30^\circ$  from  $y$  in the  $xy$ -plane. Despite these similarities, the ODFs change significantly with resolution. For example, the grouping of  $V1_{s\text{-individual}}$  and  $V3_{s\text{-individual}}$  is more pronounced in the higher-resolution data. These differences are reflected by the total shape ellipsoids (Figure 5h), and may be a result of resolution artifacts, or indicate size-dependent pore orientation. For D1263Y2, the orientation of the total shape ellipsoid is controlled by the main groupings of  $V1_{s\text{-individual}}$  and  $V3_{s\text{-individual}}$  (Figure 5i). Conversely, for D1234X,  $V2_{s\text{-total}}$  is sub-parallel to the maximum grouping of  $V3_{s\text{-individual}}$  while  $V1_{s\text{-total}}$  aligns with the maximum of a broad distribution of  $V1_{s\text{-individual}}$ . Thus, it is the absence of  $V1_{s\text{-individual}}$  rather than the presence of  $V3_{s\text{-individual}}$  that define the orientation of  $V3_{s\text{-total}}$  (Figure 5j).

For molasse sample C43Y, the  $V1_{s\text{-individual}}$  and  $V1_{s\text{-total}}$  axes are sub-parallel to  $x$ . The  $V3_{s\text{-individual}}$  and  $V3_{s\text{-total}}$  show a pronounced maximum along  $z$  (Figure 5k). Sample C334Y displays largely different ODFs for data obtained with 15 and 9  $\mu\text{m}$  resolution. The 15  $\mu\text{m}$  data show the  $V1_{s\text{-individual}}$  sub-parallel to  $x$  and  $V3_{s\text{-individual}}$  along  $z$ . Conversely, the higher-resolution data shows a concentration of  $V1_{s\text{-individual}}$  parallel to  $z$ , that is, along the preferred directions of  $V3_{s\text{-individual}}$  as identified by 15  $\mu\text{m}$  data. Also the orientation of the total shape ellipsoid is resolution-dependent, although the discrepancy is less than observed in the ODFs (Figure 5l). This observation highlights the importance of adequate resolution in XRCT studies. For sample BE42AY, the  $V1_{s\text{-individual}}$  and  $V1_{s\text{-total}}$  axes are along  $z$ . The  $V3_{s\text{-individual}}$  and  $V3_{s\text{-total}}$  are at  $\sim 30^\circ$  from  $x$  in the  $xy$ -plane (Figure 5m).

A relatively small number of pores was identified above the size threshold suitable for fabric analysis in 5256X, resulting in ODFs with many sub-maxima. As a consequence, the total shape ellipsoid is poorly defined, especially in the  $V2$ - $V3$  plane (Figure 5n). The confidence angles of the total shape ellipsoid may thus indicate the quality of the underlying XRCT data. Sample F31Z1 shows the  $V1_{s\text{-individual}}$  and  $V1_{s\text{-total}}$  axes along  $x$ . The directions for  $V3_{s\text{-individual}}$  and  $V3_{s\text{-total}}$  group at  $\sim 20^\circ$  from  $z$  in the  $yz$ -plane (Figure 5o).

**Figure 5.** Comparison of point distribution and orientation density functions (ODFs) of pore axes, bootstrapped total shape ellipsoids, and magnetic pore fabrics (MPFs) for calcarenites and molasses. ODFs include pores larger than  $4 \times 4 \times 4$  voxels to reduce resolution artifacts. Pore orientation and MPF results are shown on upper hemisphere equal area stereonet.  $V1$ ,  $V2$ , and  $V3$  indicate the maximum, intermediate and minimum axes of the total shape ellipsoid. The ellipses show the 95% confidence based on bootstrapping (Constable & Tauxe, 1990; Hext, 1963; Jelínek & Kropáček, 1978; Owens, 2000; Tauxe et al., 1998). The total shape ellipsoid with confidence ellipses is drawn using the TomoFab MATLAB code, and the red dashed line highlights the  $V1$ – $V2$  plane, that is, the foliation defined by the SPO; the lineation corresponds to the direction of  $V1$  (Petri et al., 2020). Principal susceptibility directions are shown for averaged (solid symbols), and individual datasets (open symbols). (a) Presents the comparison of point distributions and orientation density functions of pore axes and total shape ellipsoids as a function of pore size threshold for MI-1-Z3.  $P_s$  is the anisotropy degree of total shape ellipsoid. (d) Presents the comparison of point distributions and orientation density functions of pore axes and total shape ellipsoids with different pore size windows ( $\text{EqDiameter} \leq 100 \mu\text{m}$  and  $\geq 100 \mu\text{m}$ ) for MI-3-X15.

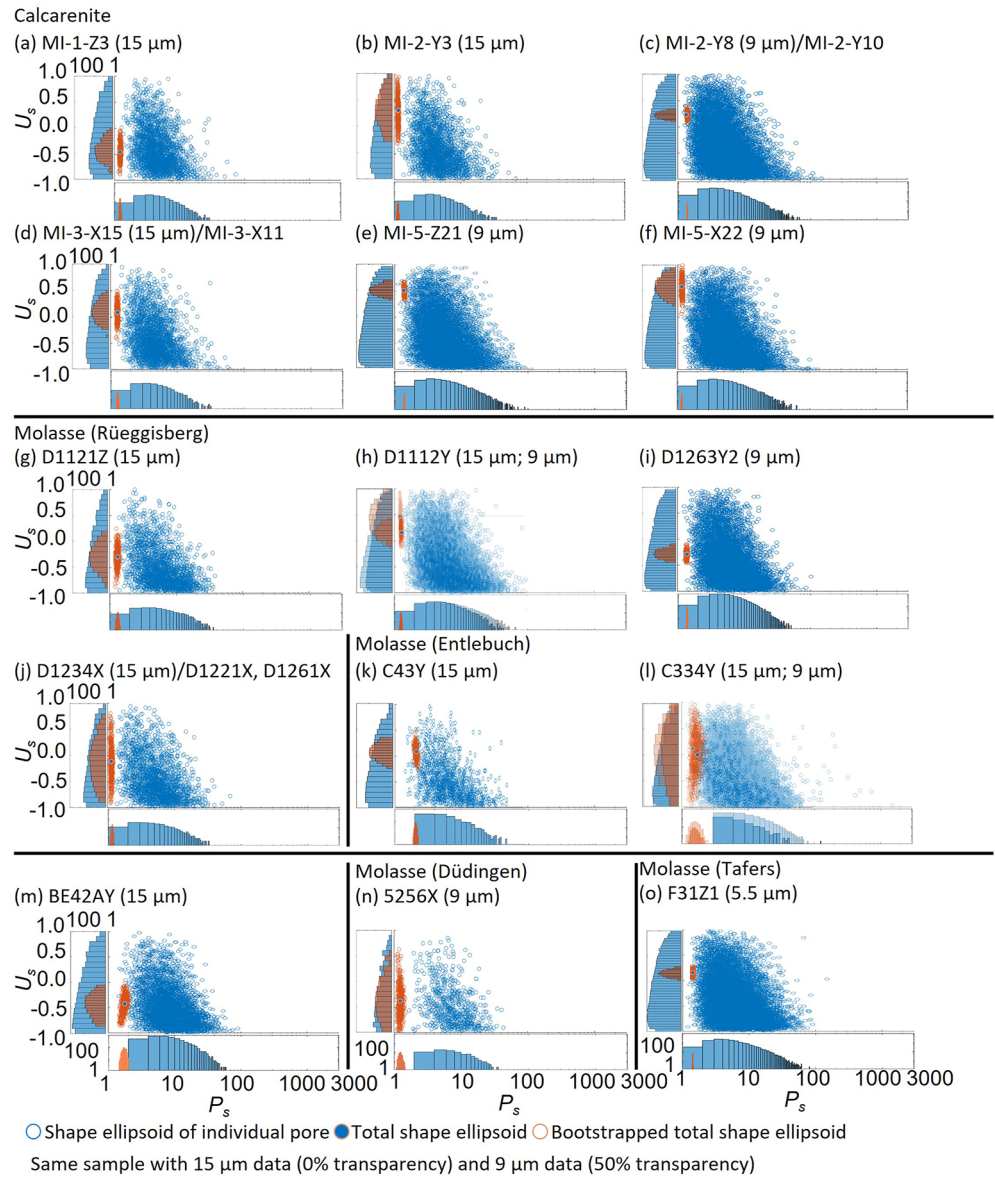


**Figure 6.** Anisotropy degree  $P_s$  ( $P_{s\text{-individual}}$ ,  $P_{s\text{-total}}$ ) and shape  $U_s$  ( $U_{s\text{-individual}}$ ,  $U_{s\text{-total}}$ ) of individual pore best-fit ellipsoids, total shape ellipsoid and bootstrapped total shape ellipsoid for all samples.

### 3.1.4. Pore Shape and Anisotropy Degree

For all samples, the individual pores present a large range of pore shapes ( $U_{s\text{-individual}}$  varies from  $-0.99$  to  $+0.99$ ) and anisotropy degrees ( $P_{s\text{-individual}}$  varies from 1.14 to 2,826). The total shape ellipsoid shows a lower anisotropy degree than the individual pores ( $P_{s\text{-total}}$  of 1.07–2.41), and a slightly smaller range of  $U_{s\text{-total}}$  values from  $-0.99$  to 0.98, which reflects the large variability in pore orientations (Figure 6).

### 3.2. MPF Results

After impregnation, the volume-normalized mean susceptibility is  $1.47\text{--}20.60 \times 10^{-3}$  SI for calcarenites and  $4.44\text{--}19.03 \times 10^{-4}$  SI for molasse sandstones (Table S4 in Supporting Information S1). The susceptibility of diluted ferrofluid is  $4.36\text{--}4.39 \times 10^{-2}$  SI (1:25 oil),  $1.16 \times 10^{-2}$  SI (1:30 resin) and  $7.11\text{--}7.39 \times 10^{-3}$  SI (1:50 resin). The MPF-derived porosity is 12.7%–47.1% for calcarenites and 3.84%–26.2% for molasse sandstones

(Table 1), reflecting  $I.E._{susc}$  of 23.7%–91.3% and 17.6%–138%, respectively.  $I.E._{susc}$  with diluted oil (52%–91.5%) is higher than one with resin mixture (23.7%–53.0%) for calcarenites (Table S4 in Supporting Information S1).

### 3.2.1. Magnetic Fabric Orientation

Not all calcarenites display well-defined MPFs; MI-1-Z3 shows no significant anisotropy (Figure 5a). Samples MI-2-Y3 (measured at 512 kHz) and MI-2-Y10 (1 kHz) display significant anisotropy, but their principal directions are poorly defined (Figures 5b and 5c). Samples MI-2-Y8, MI-3-X11, MI-5-Z21 and MI-5-X22 show significant anisotropy, and well-defined directions (Figures 5c–5f, and Table S4 in Supporting Information S1). The  $V3_{m-MPF}$  of sample MI-2-Y8 is sub-parallel to the  $z$ -axis. The  $V1_{m-MPF}$  is at  $31^\circ$  to  $x$ -axis in the  $xy$ -plane (Figure 5c). For sample MI-3-X11, the MPFs measured at different frequencies are co-axial, with largest confidence angles at 16 kHz, and  $V1_{m-MPF}$  at  $36^\circ$  to the  $y$ -axis in the  $xy$ -plane,  $V3_{m-MPF}$  sub-parallel to the  $z$ -axis (Figure 5d). For sample MI-5-Z21, the  $V1_{m-MPF}$  deviates  $24^\circ$  from the  $x$ -axis, and  $V3_{m-MPF}$  is oriented along  $z$ -axis (Figure 5e). The  $V1_{m-MPF}$  of sample MI-5-X22 is parallel to the  $x$ -axis, and  $V2_{m-MPF}$  and  $V3_{m-MPF}$  lie within the  $yz$ -plane (Figure 5f).

Most molasse samples show significant anisotropy and well-defined directions. Sample D1221X possesses significant anisotropy but poorly defined directions, and samples D1234X and D1261X have a well-defined  $V1_{m-MPF}$ , but large confidence angles in the  $V2_{m-MPF}$ – $V3_{m-MPF}$  plane (Figure 5). For sample D1121Z, the MPFs show similar orientation independent of frequency and the  $V1_{m-MPF}$ ,  $V2_{m-MPF}$  and  $V3_{m-MPF}$  are along the  $y$ -,  $x$ - and  $z$ -axes, respectively. Largest confidence angles are observed at 16 kHz (Figure 5g). The  $V1_{m-MPF}$  of sample D1112Y is  $\sim 10^\circ$  from the  $x$ -axis, and  $V2_{m-MPF}$  and  $V3_{m-MPF}$  are in a plane that is rotated ca  $10^\circ$  around  $z$  from the  $yz$ -plane (Figure 5h). Both samples D1263Y2 and D1234X show well-defined  $V1_{m-MPF}$  sub-parallel to the  $y$ -axis, and  $V2_{m-MPF}$  and  $V3_{m-MPF}$  in the  $xz$ -plane (Figures 5i and 5j). Sample D1221X and BE42AY have significant anisotropy of MPFs but poorly defined directions. Sample D1261X shows well-defined  $V2_{m-MPF}$  along  $z$ -axis, and  $V1_{m-MPF}$  and  $V3_{m-MPF}$  rotated  $\sim 30^\circ$  around the  $z$ -axis in the  $xy$ -plane (Figures 5j and 5m). The MPFs of sample C43Y in different frequencies possess the same well-defined  $V1_{m-MPF}$ ,  $V2_{m-MPF}$  and  $V3_{m-MPF}$  at  $\sim 10^\circ$  to the  $x$ ,  $y$ , and  $z$  directions, respectively (Figure 5k). Sample C334Y has well defined  $V1_{m-MPF}$  and  $V2_{m-MPF}$  in a plane rotated ca  $45^\circ$  around  $z$  from the  $xz$ -plane and  $V3_{m-MPF}$  at  $\sim 45^\circ$  to  $x$ -axis (Figure 5l). For sample F31Z1, MPF axes are well defined. The  $V1_{m-MPF}$  is at  $\sim 20^\circ$  from the  $xy$ -plane, and  $V3_{m-MPF}$  is at  $\sim 30^\circ$  to the  $z$ -axis (Figure 5o).

### 3.2.2. Anisotropy Degree and Shape of the Magnetic Fabric

The MPF anisotropy degrees of calcarenites are 1.01–1.05, and the shape values  $U_{m-MPF}$  vary between  $-0.79$  and  $0.52$  for samples with significant anisotropy. Note that the anisotropy shape is poorly defined for samples with low anisotropy and noisy data (Biedermann et al., 2013), which explains the large variability in these datasets. The molasse sandstones show higher anisotropy degrees, with  $P_{m-MPF}$  between 1.01 and 1.20, and the shape values  $U_{m-MPF}$  range from  $-0.86$  to  $0.37$ . The samples that were measured at several frequencies mostly show different  $U_{m-MPF}$  values and similar  $P_{m-MPF}$ . Conversely, sample D1121Z shows similar  $U_{m-MPF}$  values at all frequencies, but  $P_{m-MPF}$  appears to vary with measurement frequency, and is higher than for other molasse samples from the same block (Figure 7).

## 3.3. Comparison of XRCT and MPF Data

### 3.3.1. Porosities

For calcarenite, XRCT-derived porosities are 13.6%–21.3% higher than MPF-derived ones except MI-2-Y3 (10% lower), and molasse presents opposite results (0.3%–20.0% lower) except D1263Y2 and F31Z1 (5.2%–7.2% higher). MPF-derived porosities with diluted oil (29.4%–46.0%) are higher than ones with resin mixture (12.7%–28.9%) for calcarenites. For calcarenites, the XRCT-derived porosities (31%–43%) have lower variability than MPF data (12.7%–46.0%). For molasses, both methods have large variability (0.6%–16.4% for XRCT and 3.8%–25.6% for MPF) (Table 1).

### 3.3.2. Directional Comparison

For MI-2-Y3,  $V1$  and  $V3$  directions of total shape ellipsoids and MPF at 512 kHz agree with each other at 95% confidence level. Similarly, total shape ellipsoids and MPFs are generally coaxial in samples D1121Z, D1112Y, D1234X, D1261X, and D1221X. The principal directions of the total shape ellipsoid and MPF are sub-parallel in C43Y, C334Y, and BE42AY but distinct at 95% confidence. For MI-5-X22, D1263Y2, and F31Z1,  $V3$  directions

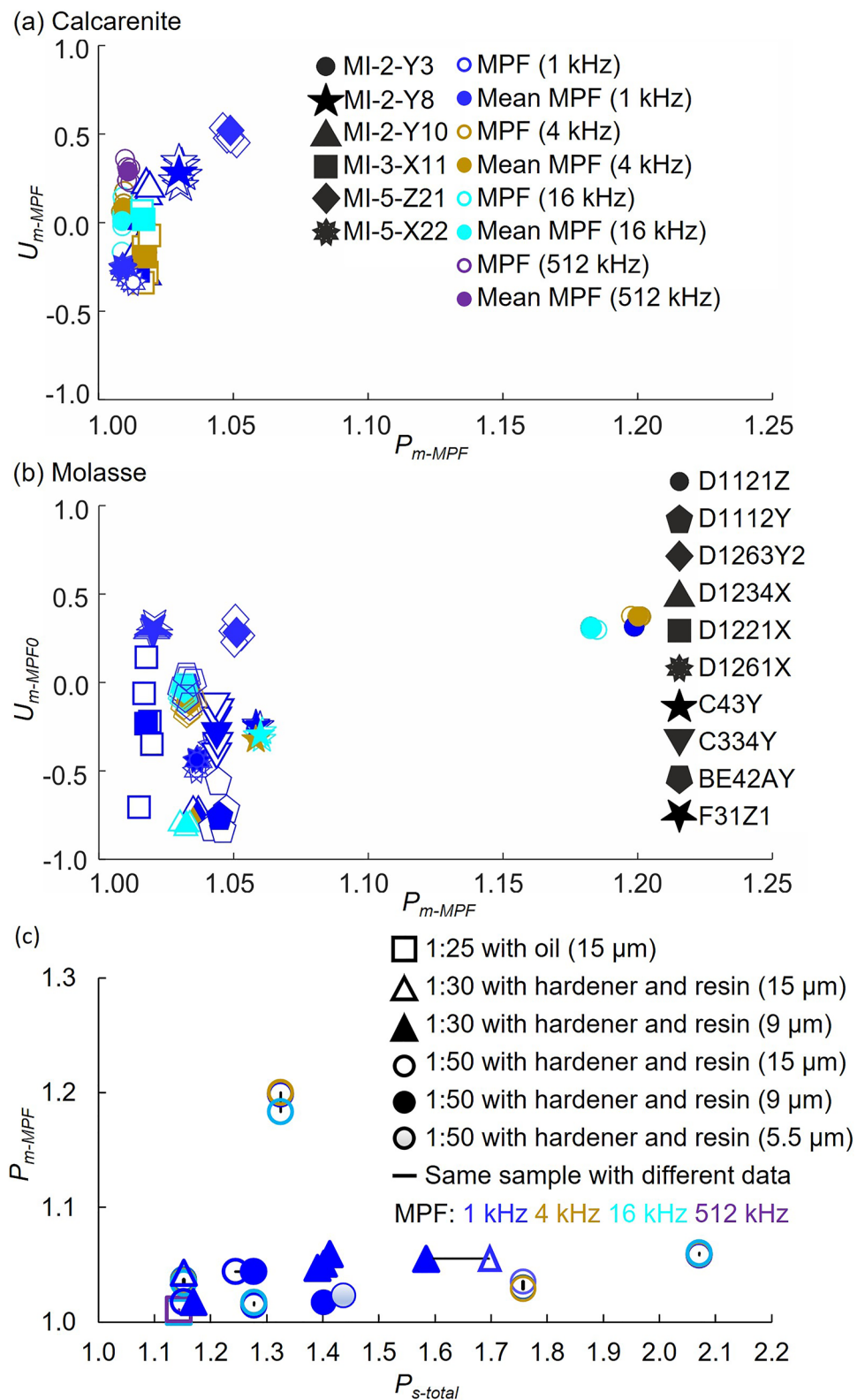


**Figure 7.** (a) and (b) Anisotropy degree and shape of the magnetic fabric. Sample MI-2-Y3 was measured at 4, 16, and 512 kHz on the SM150. MI-3-X11, D1121Z, D1234X, C43Y, and BE42AY were measured at 1 kHz, 4 and 16 kHz on the MFK1-FA. Remaining samples were measured at 1 kHz on the MFK1-FA. (c) Degree of magnetic anisotropy ( $P_{m-MPF}$ ) against anisotropy degree of total shape ellipsoid ( $P_{s-total}$ ). All samples were measured in 15  $\mu\text{m}$ , 9  $\mu\text{m}$  or 5.5  $\mu\text{m}$  X-ray computed micro-tomography and impregnated by oil-based ferrofluid (EMG 909), using different concentrations.

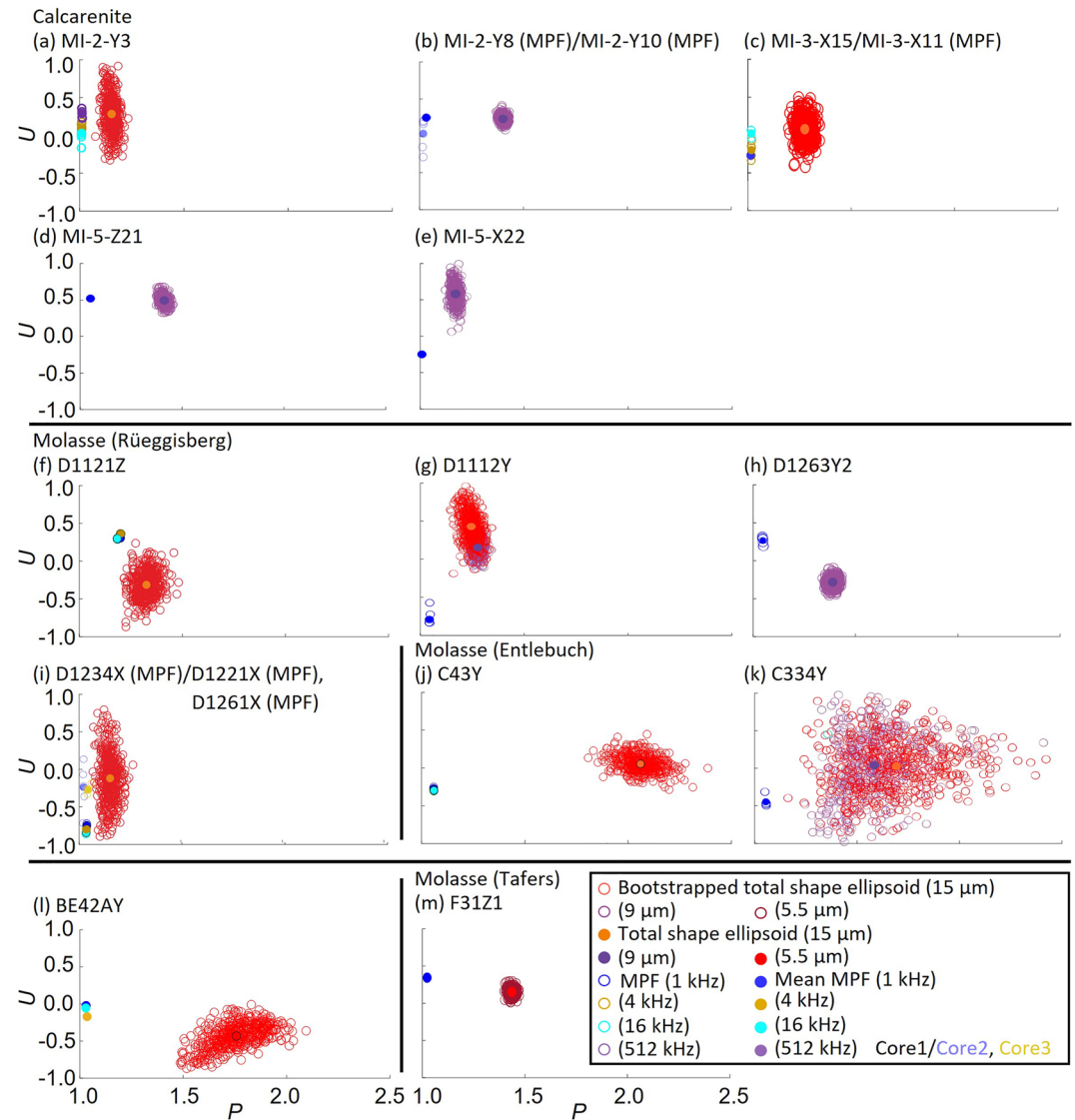


**Figure 8.** Comparison of anisotropy degree and shape derived from X-ray computed micro-tomography (total shape ellipsoid) and magnetic pore fabric datasets. Samples MI-1-Z3, MI-2-Y3 and MI-3-X15 were measured at 4 kHz, 16 and 512 kHz on the SM150. MI-3-X11, D1121Z, D1234X, C43Y, and BE42AY were measured at 1 kHz, 4 and 16 kHz on the MFK1-FA. Remaining samples were measured at 1 kHz on the MFK1-FA.

of total shape ellipsoid and MPF are similar but their  $V_1$  and  $V_2$  axes are distinct. Conversely, directions are statistically distinct at 95% confidence in samples MI-2-Y8 and MI-5-Z21 (Figure 5).

### 3.3.3. Comparison of Anisotropy Degree and Shape

The MPF anisotropy degree is lower than that of the total shape ellipsoid in all samples. It is expected that  $P_{m-MPF}$  increases with  $P_{s-total}$ , and a higher-susceptibility ferrofluid causes stronger increase. Inconsistent correlations are presented in our data, partly due to measurement uncertainty, and only few datasets existing with the same ferrofluid susceptibility and measurement frequency, hindering statistical analysis. For similar reasons, it is impossible to evaluate whether  $P_{m-MPF}$  displays a consistent frequency dependence (Figure 7). Anisotropy shapes agree within uncertainty for total shape ellipsoid and MPF in samples MI-2-Y3, MI-2-Y8, MI-5-Z21, D1234X, D1261X, D1221X, BE42AY, and F31Z1, but are different for both fabric measurements in the remaining samples (Figure 8). Comparing higher and lower resolution XRCT data suggests that both D1121Y and C334Y show similar anisotropy degree and shape at both resolutions (Figures 8g and 8k).

#### 4. Discussion

3D pore fabrics of calcarenite and molasse sandstone were investigated directly by XRCT, and indirectly by MPF. The XRCT technique is commonly used to characterize the internal structure of reservoir rocks because of non-destructiveness and 3D descriptions on pore fabrics (Cnudde & Boone, 2013; da Silva, 2018; Landis & Keane, 2010; Zeng et al., 2017). However, due to limited resolution and related artifacts, the smallest pores are unresolved by XRCT, and distinguishing isolated and connected pores is challenging because of narrow pore throats (Feser et al., 2008; Gelb et al., 2009; Zhan et al., 2009; Zubair, 2012). The voxel size is 5.5, 9 or 15  $\mu\text{m}$ , corresponding to a spatial resolution of 10'648, 46'656 or 216'000  $\mu\text{m}^3$  ( $4 \times 4 \times 4$  voxels) for characterizing pore fabrics. Selecting  $4 \times 4 \times 4$  voxels as filter was a compromise between keeping as many pores as possible and reducing resolution-related artifacts that affect the ODFs of the major and minor pore axes at the expense of losing 1%–22% of XRCT-derived pores (Table 1), decreasing the representativeness. Fabric orientations in different pore size windows show sub-parallel axes and different confidence angles, because window of smaller pores includes more unresolved micropores (Figure 5d). The comparisons of different resolutions (9 and 15  $\mu\text{m}$ ) indicate higher resolution detects more micropores, and also more small grains decreasing pore volume. One sample presents additional pores in all sizes with higher resolutions, probably because changing XRCT threshold to segment pores caused more pores resolved in all sizes. For these, different fabric orientations are observed between two datasets (Figures 5h and 5l), indicating that different pore sizes display different pore fabrics. Conversely, anisotropy degrees and shapes appear independent of resolution (Figures 6h, 6l, and 8g, 8k). This suggests that the pore shapes and aspect ratios are similar across all pore sizes, while their orientations vary.

A total shape ellipsoid is introduced to minimize the effect of resolution-related artifacts without excluding small pores, providing a more stable measurement of pore fabric. In addition to reducing artifacts, the total shape ellipsoid can also derive an average pore fabric from a poorly defined and noisy ODF, and it allows a direct comparison of pore fabrics with second-order tensor properties, such as magnetic susceptibility, permeability or thermal diffusivity. We recommend this strategy for future analyses of pore or grain shape distributions in studies about average fabric determination, or when modeling physical properties for reservoir evaluation and characterization. We expect that analyses based on total shape ellipsoids are particularly applicable to rocks with simple ellipsoidal pores. An alternative approach in need of further tests, is to use the best-fit ellipsoids of pores as input for a numerical model calculating MPFs for given pore assemblies and ferrofluid susceptibility (Biedermann, 2020). Complex pore shapes may need more sophisticated descriptions from further investigations.

The MPF method has been proposed as an efficient pore fabric characterization technique to capture pores down to 10 nm (Pfleiderer & Halls, 1993; Robion et al., 2014). If reaching this limit, it would provide insight into the fabric of small pores unresolved by XRCT. There is no linear trend between the concentration and fluid susceptibility because susceptibility is lower when using resin rather than oil for dilution (Pugnetti et al., 2021). Fluid susceptibility still varies (<4%) after correcting frequency dependence, possibly because of the discrepancy between this study and Biedermann et al. (2021), for example, time dependence. If changing corrected coefficient, all derived quantities, for example, impregnation efficiency will change. The impregnation efficiency varies largely for different samples when using the standard vacuum impregnation method commonly applied in MPF studies (Parés et al., 2016; Pugnetti et al., 2021) (Table S4 in Supporting Information S1).  $I.E._{\text{susc}}$  and MPF-derived porosities with diluted oil are higher than with resin mixture, due to higher viscosity of resin causing harder impregnation. He-pycnometer porosity is higher than MPF and XRCT-derived porosities. MPF presents higher porosity than XRCT for most molasses but opposite for most calcarenites, possibly because in the large pores, ferrofluid particles may aggregate and sediment (Figures 2b and 2d). XRCT-derived porosities for calcarenites present lower variability than ones for molasses, may due to large pores easily resolved by XRCT. Ferrofluid on the sample surface was not entirely eliminated, may causing  $I.E._{\text{susc}} > 100\%$  and MPF-derived porosity > He-pycnometer porosity in the corresponding samples and MPF-derived porosities varying for different samples and diluents. The anomalies may also result from inhomogeneous fluid, and the uncertainty in the determination of fluid susceptibility/frequency dependence, because of the time-dependent nature of fluid properties. Nevertheless, results presented here show a quantitative relationship between MPF and XRCT-derived pore fabric. Six out of 12 samples exhibit the same fabric orientation for XRCT and MPF data at 95% confidence, including only one calcarenite, probably because very weak anisotropy of calcarenite makes it impossible to interpret orientation. With very large pores, ferrofluid sedimenting to the bottom of pore may cause changes to MPF, especially for an almost isotropic sample, for example, calcarenite. The additional three samples show

sub-parallel fabric orientations, though they are distinct at 95% confidence. Three samples possess fabrics with minimum axes that are co-axial between XRCT and MPF data but one of them shows deviations in the other two axes. In the other, the orientations of  $V_1$  and  $V_2$  axes cannot be compared, as  $V_{1-s-total}$  and  $V_{2-s-total}$  directions are not statistically significant. Observed discrepancies in the XRCT and MPF fabric measures may be related to artifacts with either method, for example, incomplete or inhomogeneous impregnation may affect MPF data, and resolution artifacts affect XRCT, as evidenced by differences in the fabric obtained on the same sample when measured at different resolutions and when considering different pore size windows in the same sample. Where XRCT data at 9 and 15  $\mu\text{m}$  resolution did not agree, the higher-resolution XRCT data was compared with the MPFs, as this captures more pores, and better reflects the pores targeted by MPFs. Related to the observation that XRCT scans at different resolutions produce different pore fabric orientations, MPFs may show different fabrics as they capture smaller pores than XRCT. In this case, the investigated methods target different parts of the pore space, and thus provide complementary information when used together. Thus, discrepancies between MPF and XRCT fabric orientations in some samples indicate a variation of pore fabric with pore size, provided that other sources such as measurement uncertainty and impregnation artifacts can be excluded. To investigate this further, a complete set of XRCT data measured at different resolutions would be necessary, which may become possible after technological advancements. Until then, the agreement of XRCT and MPF fabric orientations in two thirds of the samples investigated here highlight the potential of the MPF method, and suggest that it could be useful to characterize the fabric of pores with sizes below the XRCT-resolution on standard-sized cores. Previously published empirical relationships between average pore shape and MPF, or the average pore elongation direction and the maximum principal susceptibility of the MPF (Hrouda et al., 2000; Jones et al., 2006; Pfeleiderer & Halls, 1993) are partly confirmed, and the concept of the total shape ellipsoid further expands these relationships, as it allows quantitative comparison.

The magnetic anisotropy degree is lower than the anisotropy degree of the total shape ellipsoid. This is expected, given the physics of self-demagnetization and shape anisotropy, and the low susceptibility of the ferrofluid and high measurement frequency (Biedermann, 2019; Biedermann et al., 2021; Jones et al., 2006). The relationship between pore axial ratio and MPF has been described by the equivalent pore concept (Hrouda et al., 2000), and corrections thereof (Jones et al., 2006). However, because not only the geometry of individual pores, but also their orientation and spatial arrangement influence the MPF, there is no unique and straightforward relationship and predicting MPFs for a given pore space needs numerical modeling (Biedermann, 2020). Here, no clear correlation was observed, partly because measured susceptibility decreases with increasing frequency (Biedermann et al., 2021). Therefore, higher fluid susceptibilities and measurement frequency of 1 kHz are recommended for MPF studies (Biedermann et al., 2021). Half of the samples display similar anisotropy shapes for both fabric measures within measurement uncertainty, while the others displayed discrepancies in anisotropy shape. This may be related to the different parts of the pore space captured, or an inherent difference between methods, and needs to be investigated further.

It remains to be established whether or not the MPF and total shape ellipsoid do relate to permeability. There are empirical correlations of MPF, pore fabrics and permeability anisotropy (Almqvist et al., 2011; Benson et al., 2003; Hailwood et al., 1999; Nabawy et al., 2009; Pfeleiderer & Halls, 1994). Permeability anisotropy is also a second order tensor property, and essential for reservoir characterization, but the measurement method should be improved to obtain a full tensor with estimating uncertainty and heterogeneity. Future work will need to investigate whether the total shape ellipsoids and MPFs defined here correlate clearly with laboratory-measured permeability anisotropy. This study lays the foundation for the quantitative comparison between a variety of fabric measures and second-order properties. More types of reservoir rocks and fabrics need to be analyzed for a detailed and thorough understanding of MPFs and their ability to predict pore fabrics and permeability anisotropy in the future, following the procedure outlined here.

## 5. Conclusions

The main goals of the study were (a) to establish quantitative relationships between XRCT-derived pore fabric data and MPFs, and (b) to investigate how the methods can complement each other in order to improve 3D pore space description for reservoir characterization. The comparison of pore fabrics calculated from XRCT and MPF data was accomplished by defining the total shape ellipsoid, an average measure of the pore fabric, integrating information on the pore shapes and orientation density derived from the XRCT data. The total shape ellipsoid

is mathematically represented by a second order symmetric tensor, and can thus be directly compared to second order tensor properties such as susceptibility or permeability. It is therefore useful not only in MPF studies, but also a wide range of fluid flow applications, or when predicting other physical rock properties relevant for reservoir evaluation and hydrocarbon exploitation.

Generally, a good agreement was observed between the total shape ellipsoid and MPFs in terms of fabric orientation, and partly in terms of anisotropy shape. This confirms and expands previous empirical relationships between average pore shape or preferred pore orientation with MPFs. Anisotropy degrees cannot be compared directly, because the susceptibility of the ferrofluid plays an important role in controlling the MPF anisotropy degree. Some open questions remain, including whether MPFs really are able to capture micropores (>10 nm of magnetic nanoparticle) as suggested in previous studies, and how the total shape ellipsoid is affected by resolution-artifacts and segmentation uncertainties. Nevertheless, the ability to quantitatively correlate MPF and total shape ellipsoid data will make the MPF method more useful in future applications.

### Data Availability Statement

XRCT particle analyses and MPF data obtained in this study can be obtained from <https://doi.org/10.5281/zenodo.6782552>.

### References

- Aliyu, M. D., & Chen, H. P. (2018). Enhanced geothermal system modelling with multiple pore media: Thermo-hydraulic coupled processes. *Energy*, *165*, 931–948. <https://doi.org/10.1016/j.energy.2018.09.129>
- Almqvist, B. S. G., Mainprice, D., Madonna, C., Burlini, L., & Hirt, A. M. (2011). Application of differential effective medium, magnetic pore fabric analysis, and X-ray microtomography to calculate elastic properties of porous and anisotropic rock aggregates. *Journal of Geophysical Research*, *116*(1), 1–17. <https://doi.org/10.1029/2010JB007750>
- Andrä, H., Combaret, N., Dvorkin, J., Glatt, E., Han, J., Kabel, M., et al. (2013). Digital rock physics benchmarks—Part I: Imaging and segmentation. *Computers & Geosciences*, *50*, 25–32. <https://doi.org/10.1016/j.cageo.2012.09.005>
- Andriani, G. F., & Walsh, N. (2002). Physical properties and textural parameters of calcarenitic rocks: Qualitative and quantitative evaluations. *Engineering Geology*, *67*(1–2), 5–15. [https://doi.org/10.1016/S0013-7952\(02\)00106-0](https://doi.org/10.1016/S0013-7952(02)00106-0)
- Avizo. (2020). Avizo 2020.1 User's Guide.
- Benson, P. M., Meredith, P. G., & Platzman, E. S. (2003). Relating pore fabric geometry to acoustic and permeability anisotropy in Crab Orchard sandstone: A laboratory study using magnetic ferrofluid. *Geophysical Research Letters*, *30*(19), 1–4. <https://doi.org/10.1029/2003GL017929>
- Biedermann, A. R. (2019). Magnetic pore fabrics: The role of shape and distribution anisotropy in defining the magnetic anisotropy of ferrofluid-impregnated samples. *Geochemistry, Geophysics, Geosystems*, *20*(12), 5650–5666. <https://doi.org/10.1029/2019GC008563>
- Biedermann, A. R. (2020). FinIrrSDA: A 3-D model for magnetic shape and distribution anisotropy of finite irregular arrangements of particles with different sizes, geometries, and orientations. *Journal of Geophysical Research: Solid Earth*, *125*(12), e2020JB020300. <https://doi.org/10.1029/2020JB020300>
- Biedermann, A. R., Lowrie, W., & Hirt, A. M. (2013). A method for improving the measurement of low-field magnetic susceptibility anisotropy in weak samples. *Journal of Applied Geophysics*, *88*, 122–130. <https://doi.org/10.1016/j.jappgeo.2012.10.008>
- Biedermann, A. R., Pagnetti, M., & Zhou, Y. (2021). Explaining the large variability in empirical relationships between magnetic pore fabrics and pore space properties. *Geophysical Journal International*, *227*(1), 496–517. <https://doi.org/10.1093/gji/ggab230>
- Bieniek, A., & Moga, A. (2000). An efficient watershed algorithm based on connected components. *Pattern Recognition*, *33*(6), 907–916. [https://doi.org/10.1016/S0031-3203\(99\)00154-5](https://doi.org/10.1016/S0031-3203(99)00154-5)
- Bultreys, T., De Boever, W., & Cnudde, V. (2016). Imaging and image-based fluid transport modeling at the pore scale in geological materials: A practical introduction to the current state-of-the-art. *Earth-Science Reviews*, *155*, 93–128. <https://doi.org/10.1016/j.earscirev.2016.02.001>
- Chelle-Michou, C., Do Couto, D., Moscarillo, A., Renard, P., & Rusillon, E. (2017). Geothermal state of the deep Western Alpine Molasse basin, France-Switzerland. *Geothermics*, *67*, 48–65. <https://doi.org/10.1016/j.geothermics.2017.01.004>
- Chen, F., Zheng, Q., Ding, X., Lu, S., & Zhao, H. (2020). Pore size distributions contributed by OM, clay and other minerals in over-mature marine shale: A case study of the Longmaxi shale from Southeast Chongqing, China. *Marine and Petroleum Geology*, *122*, 104679. <https://doi.org/10.1016/j.marpetgeo.2020.104679>
- Chevalier, G., Diamond, L. W., & Leu, W. (2010). Potential for deep geological sequestration of CO<sub>2</sub> in Switzerland: A first appraisal. *Swiss Journal of Geosciences*, *103*(3), 427–455. <https://doi.org/10.1007/s00015-010-0030-4>
- Ciantia, M. O., Castellanza, R., Crosta, G. B., & Hueckel, T. (2015). Effects of mineral suspension and dissolution on strength and compressibility of soft carbonate rocks. *Engineering Geology*, *184*, 1–18. <https://doi.org/10.1016/j.enggeo.2014.10.024>
- Cnudde, V., Boone, M., Dewanckele, J., Dierick, M., Van Hoorebeke, L., & Jacobs, P. (2011). 3D characterization of sandstone by means of X-ray computed tomography. *Geosphere*, *7*(1), 54–61. <https://doi.org/10.1130/GES00563.1>
- Cnudde, V., & Boone, M. N. (2013). High-resolution X-ray computed tomography in geosciences: A review of the current technology and applications. *Earth-Science Reviews*, *123*, 1–17. <https://doi.org/10.1016/j.earscirev.2013.04.003>
- Constable, C., & Tauxe, L. (1990). The bootstrap for magnetic susceptibility tensors. *Journal of Geophysical Research*, *95*(B6), 8383. <https://doi.org/10.1029/JB095iB06p08383>
- Coulson, C. A., & Nye, J. F. (1958). Physical properties of crystals. *The Mathematical Gazette*, *42*(342), 329–330. <https://doi.org/10.2307/3610487>
- da Silva, Í. B. (2018). X-Ray computed microtomography technique applied for cementitious materials: A review. *Micron*, *107*(January), 1–8. <https://doi.org/10.1016/j.micron.2018.01.006>
- David, C., Robion, P., & Louis, L. (2017). A single laboratory setup for investigating the anisotropy of both seismic and electrical properties in core samples. *Geophysical Journal International*, *210*(3), 1595–1608. <https://doi.org/10.1093/gji/ggx248>

### Acknowledgments

We are very thankful for the support from technician Sandro Bula. We would like to thank R. Castellanza from the Università degli Studi Milano Bicocca (Milano, Italy) for providing the calcarenites. Bjarne Almqvist, Philippe Robion and one anonymous reviewer are gratefully acknowledged for their thoughtful reviews which helped to improve the manuscript. The XRCT analysis in Bern was supported by the European Research Council (ERC) under the European Union's Horizon 2020 research and innovation program (grant agreement no 850530 to PL). The Bruker Skyscan 2211 at the University of Fribourg has been funded through R'Equip Swiss National Science Foundation Grant 206021\_150731. This study was funded by the Swiss National Science Foundation, project 176917 (to ARB).

- De Boever, W., Derluyn, H., Van Loo, D., Van Hoorebeke, L., & Cnudde, V. (2015). Data-fusion of high resolution X-ray CT, SEM and EDS for 3D and pseudo-3D chemical and structural characterization of sandstone. *Micron*, *74*, 15–21. <https://doi.org/10.1016/j.micron.2015.04.003>
- Donnalòia, M., Giachetta, E., Capolongo, D., & Pennetta, L. (2019). Evolution of fluvioikarst canyons in response to the Quaternary tectonic uplift of the Apulia Carbonate Platform (southern Italy): Insights from morphometric analysis of drainage basins. *Geomorphology*, *336*, 18–30. <https://doi.org/10.1016/j.geomorph.2019.03.008>
- Dullien, F. A. L. (1979). Porous media: Fluid transport and pore structure.
- Esteban, L., Géraud, Y., & Bouchez, J. L. (2006). Pore network geometry in low permeability argillites from magnetic fabric data and oriented mercury injections. *Geophysical Research Letters*, *33*(18), L18311. <https://doi.org/10.1029/2006GL026908>
- Feser, M., Gelb, J., Chang, H., Cui, H., Duerwer, F., Lau, S. H., et al. (2008). Sub-micron resolution CT for failure analysis and process development. *Measurement Science and Technology*, *19*(9), 094001. <https://doi.org/10.1088/0957-0233/19/9/094001>
- Frosch, G. P., Tillich, J. E., Haselmeier, R., Holz, M., & Althaus, E. (2000). Probing the pore space of geothermal reservoir sandstones by nuclear magnetic resonance. *Geothermics*, *29*(6), 671–687. [https://doi.org/10.1016/S0375-6505\(00\)00031-6](https://doi.org/10.1016/S0375-6505(00)00031-6)
- Gao, Z., & Hu, Q. (2018). Pore structure and spontaneous imbibition characteristics of marine and continental shales in China. *AAPG Bulletin*, *102*(10), 1941–1961. <https://doi.org/10.1306/03291817297>
- Garefalakis, P., & Schlunegger, F. (2019). Tectonic processes, variations in sediment flux, and eustatic sea level recorded by the 20 Myr old Burdigalian transgression in the Swiss Molasse basin. *Solid Earth*, *10*(6), 2045–2072. <https://doi.org/10.5194/se-10-2045-2019>
- Gelb, J., Feser, M., Tkachuk, A., Hsu, G., Chen, S., Chang, H., et al. (2009). Sub-micron X-ray computed tomography for non-destructive 3D visualization and analysis. *Microscopy and Microanalysis*, *15*(Suppl. 2), 618–619. <https://doi.org/10.1017/S1431927609093623>
- Gostick, J. T. (2017). Versatile and efficient pore network extraction method using marker-based watershed segmentation. *Physical Review E*, *96*(2), 023307. <https://doi.org/10.1103/PhysRevE.96.023307>
- Guo, B. (2019). *Well Productivity Handbook* (2nd ed., pp. 17–51). Gulf Professional Publishing. <https://doi.org/10.1016/C2018-0-03220-X>
- Gustafsson, M. G. L. (2000). Surpassing the lateral resolution limit by a factor of two using structured illumination microscopy. *Journal of Microscopy*, *198*(2), 82–87. <https://doi.org/10.1046/j.1365-2818.2000.00710.x>
- Hailwood, E. A., Bowen, D., Ding, F., Corbett, P. W. M., & Whattler, P. (1999). Characterizing pore fabrics in sediments by anisotropy of magnetic susceptibility analyses. *Geological Society, London, Special Publications*, *151*(1), 125–126. <https://doi.org/10.1144/GSL.SP.1999.151.01.12>
- Heilbronner, R., & Barrett, S. (2013). Image analysis in earth sciences. *Microstructures and Textures of Earth Materials*. <https://doi.org/10.1007/978-3-642-10343-8>
- Heintzmann, R., & Ficz, G. (2013). Breaking the resolution limit in light microscopy. *Methods in Cell Biology*, *114*(4), 525–544. <https://doi.org/10.1016/B978-0-12-407761-4.00022-1>
- Hext, G. R. (1963). The estimation of second-order tensors, with related tests and designs. *Biometrika*, *50*(3/4), 353. <https://doi.org/10.2307/2333905>
- Holzer, L., Münch, B., Iwanschitz, B., Cantoni, M., Hocker, T., & Graule, T. (2011). Quantitative relationships between composition, particle size, triple phase boundary length and surface area in nickel-cermet anodes for Solid Oxide Fuel Cells. *Journal of Power Sources*, *196*(17), 7076–7089. <https://doi.org/10.1016/j.jpowsour.2010.08.006>
- Hrouda, F., Hanak, J., & Terzijski, I. (2000). The magnetic and pore fabrics of extruded and pressed ceramic models. *Geophysical Journal International*, *142*(3), 941–947. <https://doi.org/10.1046/j.1365-246X.2000.00216.x>
- Humbert, F., Robion, P., Louis, L., Bartier, D., Ledésert, B., & Song, S. R. (2012). Magnetic inference of in situ open microcracks in sandstone samples from the Taiwan Chelungpu Fault Drilling Project (TCDFP). *Journal of Asian Earth Sciences*, *45*, 179–189. <https://doi.org/10.1016/j.jseas.2011.10.009>
- Ingham, J. P. (2010). Geomaterials under the microscope: A colour guide. <https://doi.org/10.1201/b15140>
- Jelinek, V. (1977). The statistical theory of measuring anisotropy of magnetic susceptibility of rocks and its application.
- Jelinek, V. (1981). Characterization of the magnetic fabric of rocks. *Tectonophysics*, *79*(3–4), T63–T67. [https://doi.org/10.1016/0040-1951\(81\)90110-4](https://doi.org/10.1016/0040-1951(81)90110-4)
- Jelínek, V., & Kropáček, V. (1978). Statistical processing of anisotropy of magnetic susceptibility measured on groups of specimens. *Studia Geophysica et Geodaetica*, *22*(1), 50–62. <https://doi.org/10.1007/BF01613632>
- Jezek, J., & Hrouda, F. (2007). A program for magnetic susceptibility-equivalent pore conversion. *Geochemistry, Geophysics, Geosystems*, *8*(10), Q10013. <https://doi.org/10.1029/2007GC001709>
- Jones, S., Benson, P., & Meredith, P. (2006). Pore fabric anisotropy: Testing the equivalent pore concept using magnetic measurements on synthetic voids of known geometry. *Geophysical Journal International*, *166*(1), 485–492. <https://doi.org/10.1111/j.1365-246X.2006.03021.x>
- Karimpouli, S., & Tahmasebi, P. (2019). Segmentation of digital rock images using deep convolutional autoencoder networks. *Computers & Geosciences*, *126*, 142–150. <https://doi.org/10.1016/j.cageo.2019.02.003>
- Kibria, M. G., Hu, Q., Liu, H., Zhang, Y., & Kang, J. (2018). Pore structure, wettability, and spontaneous imbibition of Woodford shale, Permian Basin, West Texas. *Marine and Petroleum Geology*, *91*, 735–748. <https://doi.org/10.1016/j.marpetgeo.2018.02.001>
- Kohl, T., Schill, E., & Baujard, C. (2010). Integrative geothermal resource assessment of the Swiss molasse basin. *Proceedings World Geothermal Congress*.
- Lai, J., Wang, G., Wang, Z., Chen, J., Pang, X., Wang, S., et al. (2018). A review on pore structure characterization in tight sandstones. *Earth-Science Reviews*, *177*, 436–457. <https://doi.org/10.1016/j.earscirev.2017.12.003>
- Landis, E. N., & Keane, D. T. (2010). X-ray microtomography. *Materials Characterization*, *61*(12), 1305–1316. <https://doi.org/10.1016/j.matchar.2010.09.012>
- Louis, L., David, C., Metz, V., Robion, P., Menéndez, B., & Kissel, C. (2005). Microstructural control on the anisotropy of elastic and transport properties in undeformed sandstones. *International Journal of Rock Mechanics and Mining Sciences*, *42*(7–8), 911–923. <https://doi.org/10.1016/j.ijrmms.2005.05.004>
- Louis, L., Robion, P., & David, C. (2004). A single method for the inversion of anisotropic data sets with application to structural studies. *Journal of Structural Geology*, *26*(11), 2065–2072. <https://doi.org/10.1016/j.jsg.2004.03.005>
- Madadi, M., & Varslot, T. K. (2009). Digital rock physics: 3D imaging of core material and correlations to acoustic and flow properties. <https://doi.org/10.1190/1.3064143>
- Madonna, C., Almqvist, B. S. G., & Saenger, E. H. (2012). Ultrasonic velocities using micro-CT imaging (pp. 1475–1482). <https://doi.org/10.1111/j.1365-246X.2012.05437.x>
- Marszałek, M., Alexandrowicz, Z., & Rzepa, G. (2014). Composition of weathering crusts on sandstones from natural outcrops and architectonic elements in an urban environment. *Environmental Science and Pollution Research*, *21*(24), 14023–14036. <https://doi.org/10.1007/s11356-014-3312-y>
- Mavris, C., Götze, J., Plötze, M., & Egli, M. (2012). Weathering and mineralogical evolution in a high Alpine soil chronosequence: A combined approach using SEM-EDX, cathodoluminescence and Nomarski DIC microscopy. *Sedimentary Geology*, *280*, 108–118. <https://doi.org/10.1016/j.sedgeo.2012.04.008>

- Mehmani, A., Verma, R., & Prodanović, M. (2020). *Pore-scale modeling of carbonates*. *Marine and petroleum geology*. Elsevier Ltd. <https://doi.org/10.1016/j.marpetgeo.2019.104141>
- Monicard, R. P. (1980). *Properties of reservoir rocks: Core analysis* (pp. 7–42). Springer. <https://doi.org/10.1007/978-94-017-5016-5>
- Nabawy, B. S., Rochette, P., & Géraud, Y. (2009). Petrophysical and magnetic pore network anisotropy of some cretaceous sandstone from Tushka Basin, Egypt. *Geophysical Journal International*, *177*(1), 43–61. <https://doi.org/10.1111/j.1365-246X.2008.04061.x>
- Oryem, M., Castellanza, R., Crosta, G. B., & Hueckel, T. (2015). Effects of mineral suspension and dissolution on strength and compressibility of soft carbonate rocks. *Engineering Geology*, *184*, 1–18. <https://doi.org/10.1016/j.enggeo.2014.10.024>
- Owens, W. H. (2000). Statistical applications to second-rank tensors in magnetic fabric analysis. *Geophysical Journal International*, *142*(2), 527–538. <https://doi.org/10.1046/j.1365-246X.2000.00174.x>
- Parés, J. M., Miguens, L., & Saiz, C. (2016). Characterizing pore fabric in sandstones with magnetic anisotropy methods: Initial results. *Journal of Petroleum Science and Engineering*, *143*, 113–120. <https://doi.org/10.1016/j.petrol.2016.02.028>
- Petri, B., Almqvist, B. S. G., & Pistone, M. (2020). 3D rock fabric analysis using micro-tomography: An introduction to the open-source Tomo-Fab MATLAB code. *Computers & Geosciences*, *138*, 104444. <https://doi.org/10.1016/j.cageo.2020.104444>
- Pfleiderer, S., & Halls, H. C. (1990). Magnetic susceptibility anisotropy of rocks saturated with ferrofluid: A new method to study pore fabric? *Physics of the Earth and Planetary Interiors*, *65*(1–2), 158–164. [https://doi.org/10.1016/0031-9201\(90\)90083-A](https://doi.org/10.1016/0031-9201(90)90083-A)
- Pfleiderer, S., & Halls, H. C. (1993). Magnetic pore fabric analysis: Verification through image autocorrelation. *Journal of Geophysical Research*, *98*(B3), 4311–4316. <https://doi.org/10.1029/92JB01851>
- Pfleiderer, S., & Halls, H. C. (1994). Magnetic pore fabric analysis: A rapid method for estimating permeability anisotropy. *Geophysical Journal International*, *116*(1), 39–45. <https://doi.org/10.1111/j.1365-246X.1994.tb02125.x>
- Pini, R. (2016). Moving across scales: A quantitative assessment of X-ray CT to measure the porosity of rocks. *Journal of Porous Materials*, *23*(2), 325–338. <https://doi.org/10.1007/s10934-015-0085-8>
- Polesel, A., Ramponi, G., & Mathews, V. J. (2000). Image enhancement via adaptive unsharp masking. *IEEE Transactions on Image Processing*, *9*(3), 505–510. <https://doi.org/10.1109/83.826787>
- Pugnetti, M., Zhou, Y., & Biedermann, A. R. (2021). Experimental improvements for ferrofluid impregnation of rocks using directional forced impregnation methods: Results on natural and synthetic samples. <https://doi.org/10.5194/egusphere-egu21-14695>
- Pugnetti, M., Zhou, Y., & Biedermann, A. R. (2022). *Ferrofluid impregnation efficiency and its spatial variability in natural and synthetic porous media: Implications for magnetic pore fabric studies*. *Transport in Porous Media*.
- Reed, S. J. B. (2005). Electron microprobe analysis and scanning electron microscopy in geology. <https://doi.org/10.1017/CBO9780511610561>
- Robion, P., David, C., Dautriat, J., Colombier, J. C., Zinsmeister, L., & Collin, P. Y. (2014). Pore fabric geometry inferred from magnetic and acoustic anisotropies in rocks with various mineralogy, permeability and porosity. *Tectonophysics*, *629*(C), 109–122. <https://doi.org/10.1109/TITS.2015.2426955>
- Rybach, L. (2019). Geothermal potential of Sedimentary Basins, especially of the Swiss Molasse Basin. *Foldtani Kozlony*, *149*(3), 401–414. <https://doi.org/10.23928/foldt.kozl.2019.149.4.401>
- Schegg, R., Leu, W., Cornford, C., & Allen, P. A. (1997). New coalification profiles in the molasse basin of Western Switzerland: Implications for the thermal and geodynamic evolution of the Alpine foreland. *Eclogae Geologicae Helveticae*, *90*(1), 79–96. <https://doi.org/10.5169/seals-168146>
- Skyscan, N. V. (2011). NRecon User Manual.
- Soille, P. (2000). Morphological image analysis: Principles and applications. *Sensor Review*, *20*, 3. <https://doi.org/10.1108/sr.2000.08720cae.001>
- Sommaruga, A., Eichenberger, U., & Marillier, F. (2012). Seismic Atlas of the Swiss Molasse Basin (Vol. 90).
- Strobel, N. K. (1996). Nonlinear unsharp masking methods for image contrast enhancement. *Journal of Electronic Imaging*, *5*(3), 353. <https://doi.org/10.1117/12.242618>
- Sun, H., Vega, S., & Tao, G. (2017). Analysis of heterogeneity and permeability anisotropy in carbonate rock samples using digital rock physics. *Journal of Petroleum Science and Engineering*, *156*, 419–429. <https://doi.org/10.1016/j.petrol.2017.06.002>
- Sun, P., Xu, H., Zhu, H., Jia, L., Hu, X., Fang, H., et al. (2021). Investigation of pore-type heterogeneity and its control on microscopic remaining oil distribution in deeply buried marine clastic reservoirs. *Marine and Petroleum Geology*, *123*, 104750. <https://doi.org/10.1016/j.marpetgeo.2020.104750>
- Tauxe, L., Gee, J. S., & Staudigel, H. (1998). Flow directions in dikes from anisotropy of magnetic susceptibility data: The bootstrap way. *Journal of Geophysical Research*, *103*(B8), 17775–17790. <https://doi.org/10.1029/98jb01077>
- Thomson, P. R., Aituar-Zhakupova, A., & Hier-Majumder, S. (2018). Image segmentation and analysis of pore network geometry in two natural sandstones. *Frontiers of Earth Science*, *6*, 58. <https://doi.org/10.3389/feart.2018.00058>
- Thorpe, A. N., Senftle, F. E., Holt, M., & Grant, J. (2016). Electron microscopy studies of low concentrations of nanoscale Fe<sub>3</sub>O<sub>4</sub> particles in epoxy resin.
- Vázquez, M. A., Galán, E., Ortiz, P., & Ortiz, R. (2013). Digital image analysis and EDX SEM as combined techniques to evaluate salt damp on walls. *Construction and Building Materials*, *45*, 95–105. <https://doi.org/10.1016/j.conbuildmat.2013.03.067>
- Wagner, R., Kühn, M., Meyn, V., Pape, H., Vath, U., & Clauser, C. (2005). Numerical simulation of pore space clogging in geothermal reservoirs by precipitation of anhydrite. *International Journal of Rock Mechanics and Mining Sciences*, *42*(7–8), 1070–1081. <https://doi.org/10.1016/j.ijrmms.2005.05.008>
- Wang, F. P., Reed, R. M., John, A., & Katherine, G. (2009). Pore networks and fluid flow in gas shales. In *Proceedings: SPE Annual Technical Conference and Exhibition*. <https://doi.org/10.2118/124253-ms>
- Wirth, S. B., Carlier, C., Cochand, F., Hunkeler, D., & Brunner, P. (2020). Lithological and tectonic control on groundwater contribution to stream discharge during low-flow conditions. *Water (Switzerland)*, *12*(3), 821. <https://doi.org/10.3390/w12030821>
- Yang, R., Hao, F., He, S., He, C., Guo, X., Yi, J., et al. (2017). Experimental investigations on the geometry and connectivity of pore space in organic-rich Wufeng and Longmaxi shales. *Marine and Petroleum Geology*, *84*, 225–242. <https://doi.org/10.1016/j.marpetgeo.2017.03.033>
- Yang, R., Hu, Q., He, S., Hao, F., Guo, X., Yi, J., & He, X. (2018). Pore structure, wettability and tracer migration in four leading shale formations in the Middle Yangtze Platform, China. *Marine and Petroleum Geology*, *89*, 415–427. <https://doi.org/10.1016/j.marpetgeo.2017.10.010>
- Yang, Y., Wang, K., Zhang, L., Sun, H., Zhang, K., & Ma, J. (2019). Pore-scale simulation of shale oil flow based on pore network model. *Fuel*, *251*, 683–692. <https://doi.org/10.1016/j.fuel.2019.03.083>
- Zeng, J., Feng, X., Feng, S., Zhang, Y., Qiao, J., & Yang, Z. (2017). Influence of tight sandstone micro-nano pore-throat structures on petroleum accumulation: Evidence from experimental simulation combining x-ray tomography. *Journal of Nanoscience and Nanotechnology*, *17*(9), 6459–6469. <https://doi.org/10.1166/jnn.2017.14514>

- Zhan, X., Schwartz, L., Smith, W., Toksöz, N., & Morgan, D. (2009). Pore scale modeling of rock properties and comparison to laboratory measurements. In *79th Society of Exploration Geophysicists International Exposition and Annual Meeting 2009, SEG 2009*, 500, 1935–1939. <https://doi.org/10.1190/1.3255234>
- Zhang, J., Liu, G., Torsaeter, O., Tao, S., Jiang, M., Li, G., & Zhang, S. (2020). Pore-throat structure characteristics and its effect on flow behavior in Gaotaizi tight siltstone reservoir, northern Songliao Basin. *Marine and Petroleum Geology*, 122, 104651. <https://doi.org/10.1016/j.marpetgeo.2020.104651>
- Zhang, P., Hu, L., Meegoda, J. N., & Gao, S. (2015). Micro/Nano-pore network analysis of gas flow in shale matrix. *Scientific Reports*, 5(1), 13501. <https://doi.org/10.1038/srep13501>
- Zhang, Z., Ma, B., Ranjith, P. G., Yang, S., & Zhou, L. (2020). Indications of risks in geothermal systems caused by changes in pore structure and mechanical properties of granite: An experimental study. *Bulletin of Engineering Geology and the Environment*, 79(10), 5399–5414. <https://doi.org/10.1007/s10064-020-01901-z>
- Zubair, M. (2012). Digital rock physics for fast and accurate special core analysis in carbonates. In *New Technologies in the Oil and Gas Industry*. <https://doi.org/10.5772/52949>